

AD-A058 814

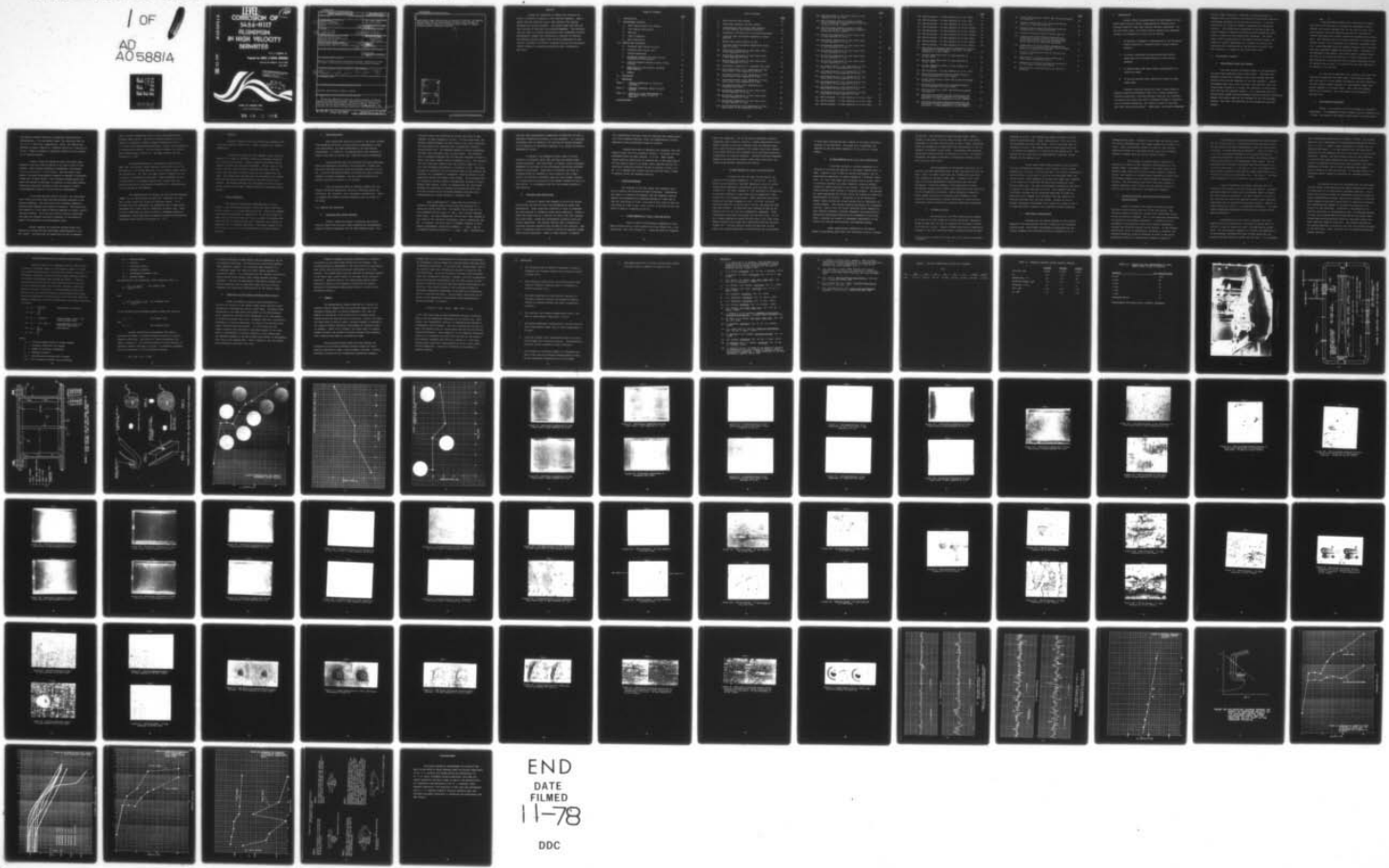
OCEAN CITY RESEARCH CORP N J  
CORROSION OF 5456-H117 ALUMINUM IN HIGH VELOCITY SEAWATER. (U)  
JUN 78 G A GEHRING  
N00014-77-C-0431

NL

UNCLASSIFIED

OCR-ONR-1

1 OF  
AD  
A058814



END  
DATE  
FILED  
11-78  
DDC

AD A0 58814

DDC FILE COPY

LEVEL II  
CORROSION OF  
5456-H117  
ALUMINUM  
IN HIGH VELOCITY  
SEAWATER

By G. A. GEHRING, JR.

Prepared for OFFICE of NAVAL RESEARCH

Contract No. N00014 - 77-C-0431

June 1978

This document has been approved  
for public release and sale; its  
distribution is unlimited.

DDC  
REF ID: A642116  
SEP 20 1978  
OCEAN CITY RESEARCH CORP.



OCEAN CITY RESEARCH CORP.

PSC PROFESSIONAL SERVICES GROUP, INC.  
A Member of the Corporate Family of PHILADELPHIA SUBURBAN CORPORATION

78 09 06 026

## Unclassified

SECURITY CLASSIFICATION OF THIS PAGE (When Data Entered)

REPORT DOCUMENTATION PAGE		READ INSTRUCTIONS BEFORE COMPLETING FORM
1. REPORT NUMBER	2. GOVT ACCESSION NO.	3. RECIPIENT'S CATALOG NUMBER
4. TITLE (and Subtitle) Corrosion of 5456-H117 Aluminum in High Velocity Seawater.		5. TYPE OF REPORT & PERIOD COVERED Final, 6/77 to 6/78
7. AUTHOR(s) G. A. Gehring, Jr.		6. PERFORMING ORG. REPORT NUMBER OCR-ONR-1
8. PERFORMING ORGANIZATION NAME AND ADDRESS Ocean City Research Corp. Tennessee Avenue & Beach Thorofare Ocean City, NJ 08226		10. PROGRAM ELEMENT, PROJECT, TASK AREA & WORK UNIT NUMBERS 12 87 P.
11. CONTROLLING OFFICE NAME AND ADDRESS Office of Naval Research Metallurgy Program Office, Code 471, Arlington, Virginia 22217		12. REPORT DATE Jun 1978
14. MONITORING AGENCY NAME & ADDRESS (if different from Controlling Office)		13. NUMBER OF PAGES 83
15. SECURITY CLASS. (of this report) Unclassified		
15a. DECLASSIFICATION/DOWNGRADING SCHEDULE		
16. DISTRIBUTION STATEMENT (of this Report) Approved for public release; distribution unlimited. Reproduction in whole or in part is permitted for any purpose of the United States Government.		
17. DISTRIBUTION STATEMENT (of the abstract entered in Block 20, if different from Report) 9 Final rep. Jun 77 - Jun 78,		
18. SUPPLEMENTARY NOTES		
19. KEY WORDS (Continue on reverse side if necessary and identify by block number) Corrosion, High Velocity, Seawater, Aluminum		
20. ABSTRACT (Continue on reverse side if necessary and identify by block number) A study was undertaken to examine the corrosion behavior of 5456-H117 aluminum in high velocity seawater. Experimental data was obtained using a high velocity flow channel operated with natural seawater. The results show that both the rate and mode of corrosion are velocity-dependent. The corrosion rate was shown to increase significantly with increasing velocity. -7 over		

Unclassified

SECURITY CLASSIFICATION OF THIS PAGE (When Data Entered)

Morphological changes were observed as a function of velocity. The observed changes suggest that the basic mechanism for high velocity corrosion of 5456-H117 aluminum involves film disruption/removal leading to enhanced micropitting about intermetallic particles.

ACCESSION for		
NTIS	Wide Section	<input checked="" type="checkbox"/>
DDC	Blank Section	<input type="checkbox"/>
UNANNOUNCED		<input type="checkbox"/>
JUSIFICATION		
BY		
DISTRIBUTION/AVAILABILITY CODES		
		SPECIAL
A		

SECURITY CLASSIFICATION OF THIS PAGE (When Data Entered)

## ABSTRACT

A study was undertaken to examine the corrosion behavior of 5456-H117 aluminum in high velocity seawater. Experimental data was obtained using a high velocity flow channel operated with natural seawater. The results show that both the rate and mode of corrosion are velocity-dependent. The corrosion rate was shown to increase significantly with increasing velocity. Morphological changes were observed as a function of velocity. The observed changes suggest that the basic mechanism for high velocity corrosion of 5456-H117 aluminum involves film disruption/ removal leading to enhanced micropitting about intermetallic particles.

TABLE OF CONTENTS

	<u>PAGE</u>
I. INTRODUCTION. . . . .	1
II. EXPERIMENTAL APPROACH. . . . .	2
A. Water Wheel Versus Flow Channel. . . . .	2
B. Flow Channel Description . . . . .	3
C. Material . . . . .	6
D. Time of Exposure. . . . .	6
E. Data Acquisition. . . . .	7
III. RESULTS AND DISCUSSION . . . . .	7
A. Corrosion Rate Versus Velocity . . . . .	7
B. Corrosion Rate Versus Time . . . . .	9
C. Surface Morphology . . . . .	10
D. Corrosion Potential and Polarization Resistance Versus Velocity . . . . .	15
E. Limiting Oxygen Diffusion Current Versus Velocity . . . . .	18
F. Comparison of Flow Channel and Water Wheel Results. . . . .	20
G. Summary. . . . .	21
IV. CONCLUSIONS . . . . .	23
V. REFERENCES . . . . .	25
TABLE I - TYPICAL COMPOSITION OF 5456-H117 ALUMINUM. . . . .	27
TABLE II - SEAWATER CHEMISTRY DURING VELOCITY STUDIES . . . . .	28
TABLE III - RESULTS OF GLOSS MEASUREMENTS ON TEST PANELS AFTER 35 DAYS AT VELOCITY. . . . .	29
ACKNOWLEDGEMENT . . . . .	78

LIST OF FIGURES

	<u>PAGE</u>
1. High Velocity Flow Channel . . . . .	30
2. Simplified Schematic of Flow Channel. . . . .	31
3. Cross-Section View of Test Panel Mounted In Flow Channel (Low Velocity Section) . . . . .	32
4. Preparation and Mounting of Platinum Electrodes . . .	33
5. Corrosion Rate and Surface Appearance Versus Velocity . . . . .	34
6. Weight Loss Versus Time At 18 m/s. . . . .	35
7. Corrosion Rate and Surface Appearance Versus Time at 18 m/s . . . . .	36
8a. Macroscopic Appearance of Test Panel After 2 Days Exposure at 18 m/s . . . . .	37
8b. Macroscopic Appearance of Test Panel After 2 Days Exposure at 9 m/s. . . . .	37
8c. Macroscopic Appearance of Test Panel After 2 days Exposure at 3 m/s. . . . .	38
8d. Macroscopic Appearance of Unexposed Test Panel . .	38
9a. Low Magnification (4.5x) Appearance of Test Panel After 2 Days Exposure at 18 m/s . . . . .	39
9b. Low Magnification (4.5x) Appearance of Test Panel After 2 Days Exposure at 9 m/s. . . . .	39
9c. Low Magnification (4.5x) Appearance of Test Panel After 2 Days Exposure at 3 m/s. . . . .	40
9d. Low Magnification (4.5x) Appearance of Unexposed Test Panel . . . . .	40
10a. Macroscopic Appearance of Test Panel After 14 Days Exposure at 18 m/s . . . . .	41
10b. Macroscopic Appearance of Test Panel After 14 Days Exposure at 9 m/s . . . . .	41
10c. Macroscopic Appearance of Test Panel After 14 Days Exposure at 3 m/s . . . . .	42
11a. Low Magnification (4.5x) Appearance of Test Panel After 14 Days Exposure at 18 m/s . . . . .	43

	<u>PAGE</u>
11b. SEM Micrograph of Test Panel After 14 Days Exposure at 18 m/s (55x) . . . . .	43
12a. SEM Micrograph Showing Crazing of Oxide Layer Downstream of Intermetallic Particles - 14 Days at 18 m/s (1000x) . . . . .	44
12b. SEM Micrograph Showing Crazing of Oxide Layer Downstream of Intermetallic Particle - 14 Days at 18 m/s (1000x) . . . . .	45
13a. Macroscopic Appearance of Test Panel After 35 Days Exposure at 18 m/s . . . . .	46
13b. Macroscopic Appearance of Test Panel After 35 Days Exposure at 15 m/s . . . . .	46
13c. Macroscopic Appearance of Test Panel After 35 Days Exposure at 12 m/s . . . . .	47
13d. Macroscopic Appearance of Test Panel After 35 Days Exposure at 9 m/s . . . . .	47
13e. Macroscopic Appearance of Test Panel After 35 Days Exposure at 6 m/s . . . . .	48
13f. Macroscopic Appearance of Test Panel After 35 Days Exposure at 3 m/s . . . . .	49
14a. Low Magnification (4.5x) Appearance of Test Panel After 35 Days Exposure at 18 m/s . . . . .	49
14b. Low Magnification (4.5x) Appearance of Test Panel After 35 Days Exposure at 15 m/s . . . . .	49
14c. Low Magnification (4.5x) Appearance of Test Panel After 35 Days Exposure at 12 m/s . . . . .	50
14d. Low Magnification (4.5x) Appearance of Test Panel After 35 Days Exposure at 9 m/s . . . . .	50
14e. Low Magnification (4.5x) Appearance of Test Panel After 35 Days Exposure at 6 m/s . . . . .	51
14f. Low Magnification (4.5x) Appearance of Test Panel After 35 Days Exposure at 3 m/s . . . . .	51
15a. SEM Micrograph - 35 Days Exposure at 18 m/s (55x) .	52
15b. SEM Micrograph - 35 Days Exposure at 15 m/s (55x) .	52
15c. SEM Micrograph - 35 Days Exposure at 12 m/s (55x) .	53

	<u>PAGE</u>
15d. SEM Micrograph - 35 Days Exposure at 9 m/s (55x) . . . . .	53
15e. SEM Micrograph - 35 Days Exposure at 6 m/s (55x) . . . . .	54
15f. SEM Micrograph - 35 Days Exposure at 3 m/s (55x) . . . . .	54
16. SEM Micrograph - 35 Days Exposure at 18 m/s (1000x) . . . . .	55
17a. SEM Micrograph - 35 Days Exposure at 15 m/s (1000x) . . . . .	56
17b. SEM Micrograph - 35 Days Exposure at 15 m/s (1000x) . . . . .	56
18a. SEM Micrograph - 35 Days Exposure at 12 m/s (300x) . . . . .	57
18b. SEM Micrograph - 35 Days Exposure at 12 m/s (1000x) . . . . .	57
19. SEM Micrograph - 35 Days Exposure at 6 m/s (1000x) . . . . .	58
20. SEM Stereo Micrograph Showing Preferential Pitting Downstream of Intermetallic Particles - 35 Days Exposure at 15 m/s (1000x) . . . . . . . . . . .	59
21. Surface Appearance After 22 Days Exposure at 30 m/s (125x) . . . . . . . . . . . . . . . . .	60
22. Surface Appearance After 22 Days Exposure at 30 m/s (250x) . . . . . . . . . . . . . . . . .	60
23. Surface Appearance After 22 Days Exposure at 30 m/s (1200x) . . . . . . . . . . . . . . . . .	61
24. SEM Micrograph - 22 Days Exposure at 30 m/s (55x) . . . . .	61
25. SEM Stereo Micrograph Showing Random Macropit - 22 Days Exposure at 30 m/s (250x) . . . . . . . . .	62
26. Higher Magnification (500x) SEM Stereo Micrograph of Figure 25. . . . . . . . . . . . . . . . .	63
27. SEM Stereo Micrograph Showing Random Macropit - 22 Days Exposure at 30 m/s (250x) . . . . . . . . .	64
28. High Magnification (500x) SEM Stereo Micrograph of Figure 27. . . . . . . . . . . . . . . . .	65
29. SEM Stereo Micrograph Showing Micropitting and Preferential Attack Downstream of Intermetallic Particles - 22 Days Exposure at 30 m/s (1000x) . . . . .	66
30. SEM Stereo Micrograph Showing Micropitting and Preferential Attack Downstream of Intermetallic Particles - 22 Days Exposure at 30 m/s (1000x) . . . . .	67

	<u>PAGE</u>
31. Higher Magnification (3000x) SEM Stereo Micrograph of Figure 30. . . . .	68
32. Surface Profile Trace with Stylus Traversing Parallel to Rolling Direction . . . . .	69
33. Surface Profile Trace with Stylus Traversing Perpendicular to Rolling Direction . . . . .	70
34. Average Corrosion Potential Versus Velocity . . . . .	71
35. Polarization Diagram Showing the Effect of Increasing Velocity on the Diffusion-Limited Anodic Polarization Curve and the Resulting Active Shift in the Corrosion Potential. . . . .	72
36. Comparison of Corrosion Rates Determined by Weight Loss and Polarization Resistance Measurements as a Function of Velocity . . . . .	73
37. Cathodic Polarization Curves On Platinum For 0 thru 18 m/s . . . . .	74
38. Comparison of Corrosion Rates Determined In Flow Channel Versus Water Wheel . . . . .	75
39. Comparison of Corrosion Potentials Determined In Flow Chanel Versus Water Wheel. . . . .	76
40. High Velocity Corrosion/Erosion of 5456-H117 Aluminum . . . . .	77

## I. INTRODUCTION

Current efforts directed toward the development of high speed ships require a better understanding of aluminum alloy corrosion behavior under high velocity seawater conditions. For the past three years, the Office of Naval Research has sponsored research, the objectives of which are as follows:

1. To develop a fundamental understanding of the corrosion/erosion behavior of aluminum alloys in high velocity seawater.
2. To better understand the rate-controlling factors associated with corrosion/erosion in high velocity seawater.
3. To develop data that might enable establishment of a predictive model.
4. To provide relevant data required for design of high speed ships.

Research conducted during the first 2 years sought to develop various electrochemical data (e.g. pitting potentials, corrosion potentials, limiting diffusion currents) as a function of velocity and relate this data to observed changes in corrosion rate and surface morphology. The results of much of this work have been reported previously.<sup>1</sup> Essentially, the results suggested

that at higher velocities, corrosion of aluminum alloys in seawater does not conform to the classical pitting mode generally found under quiescent or low velocity conditions. It was observed that pit intensity tended to decrease with increasing velocity. This effect was rationalized on the basis that the anolyte chemistry required to sustain pitting becomes more difficult to attain as flow becomes more turbulent. The third year's effort concentrated on developing a better insight into changes in surface morphology as a function of velocity and resolving some uncertainties of the previous two years' work. The following is a report of the third year's work.

## II. EXPERIMENTAL APPROACH

### A. Water Wheel Versus Flow Channel

The high velocity corrosion studies in the preceeding two years were conducted using a water wheel<sup>1</sup>. Specimens were exposed to mixed flow (impinging flow on the leading edge and parallel flow over the remainder of the test specimen). Because impingement-type flow is more corrosive than parallel flow, the leading edge corroded at a higher rate resulting in uneven metal loss over the test specimen surface. It is suspected that this uneven attack caused velocity-dependent galvanic potential differences between the leading edge and the remainder of the test specimen surface. This made interpretation of electrochemical data more complex.

A test specimen incorporating a non-metallic leading edge could have been used to overcome the impingement effect. However, the overall specimen size (25 mm. wide x 50 mm. long) was limited in the water wheel and the use of a non-metallic leading edge would have further reduced the exposed metal surface area. Test specimen size is of concern because it is questionable whether uniform, fully developed flow conditions (boundary layer, etc.) were established over the exposed surface of the relatively small-size specimens imposed by the water wheel. Attachment of the specimen to the support strut also creates a boundary where the flow is not easily defined while, at high velocities, the wake created by a test specimen can be carried completely around the spinning tub so that it is possible for the test specimen to be exposed to its own wake.

To overcome the specimen size, boundary, and mixed flow constraints imposed by the water wheel, high velocity studies were initiated in a flow channel available at the OCRC laboratory. The flow channel permits exposure of significantly larger test panels compared to the water wheel. Thus, edge and boundary effects are minimized. Also, the panels are only exposed to parallel flow.

#### B. Flow Channel Description

Figure 1 is a picture of the flow channel as originally constructed. It accommodated natural seawater velocity studies up to  $\approx 18$  m/s. The width of the channel cross-section is varied along

the length to permit testing at 6 different flow velocities simultaneously. For the subject study, the velocities were 18, 15, 12, 9, 6 and 3 m/s, respectively. Later, the channel was modified to permit testing in a separate section at a velocity of 30 m/s. Figure 2 presents a simplified schematic of the channel as it currently exists.

Figure 3 shows the method by which test panels were mounted in the low velocity section (3 m/s thru 18 m/s) of the channel. Each velocity subsection accommodated 5 test panels (17.5 cm x 25.5 cm x  $\approx$  1.3 cm thick). The test panels were spaced 5 cm apart using phenolic spacers to maintain a continuous center wall in each section. The interface between spacer and panel was matched as precisely as possible to avoid edge effects. Electrical leads were attached to each test panel to permit electrochemical potential and polarization measurements.

In the high velocity section (30 m/s), the test panels were fitted into slots which had been precisely machined in the acrylic sidewalls. The test panels were carefully shimmed to minimize edge mismatch and eliminate cavitation. The panels were also seated in a thin layer of potting compound to prevent crevice corrosion effects. As in the low velocity section, provisions were made for external electrical connection to the panels to permit the acquisition of electrochemical data.

Natural seawater is circulated through either test section by a double-suction centrifugal pump powered by a 100 H.P. motor. The flow rate can exceed 300 l/s and is measured

using a factory-calibrated 316 SS orifice plate/differential pressure gauge set-up. The rate of seawater make-up into the channel is adjusted to control seawater temperature within  $\pm$  2.5°C while being maintained sufficiently high to avoid stagnation or concentration effects. For the subject studies, the make-up rate varied between 2 and 5 l/s. The make-up water was also filtered to  $<1$  JTU.

All wetted materials in the channel, except for the pump (cast iron casing, bronze impeller) and orifice plate, are non-metallic. All wetted materials in the seawater supply system are non-metallic. The cast iron pump casing is coated with coal tar-epoxy and cathodically protected. These procedures as well as maintenance of an adequate make-up rate insured that the results would not be influenced by atypically high concentrations of trace metals in the seawater.

The dimensions of the channel are such that the Reynolds number,  $Re$ , at each velocity is about  $10^6$ , resulting in a flow that is well within the transition turbulent region. It is believed that this represents the maximum  $Re$  that is practically achievable for a high velocity laboratory corrosion test. High  $Re$  flow is desirable in order to obtain a reasonable degree of hydrodynamic similitude between laboratory conditions and service conditions (high velocity ship where  $Re > 10^9$ ).

### C. Material

5456-H117 aluminum alloy test panels were prepared from certified commerical alloy plate. Table I presents the typical composition.

A platinum electrode was also exposed in each velocity subsection in order to determine limiting  $O_2$  diffusion currents as a function of velocity. Figure 4 depicts the method used to prepare and mount the platinum electrodes. 500 mm. long x 3 mm. wide x .127 mm. thick strips of platinum foil were cigarette-rolled and then cast in acrylic resin so as to expose only the edge. The acrylic-cast platinum was then polished on the exposed edge side and solvent-cemented flush in the side wall of the channel. The mounted specimen was re-polished so as to provide a smooth surface with minimal mismatch between the platinum and the acrylic.

### D. Time of Exposure

The velocity studies were conducted over a 35 day period in the low velocity section (18 m/s and lower) and over a 22 day interval in the high velocity section. Panels were removed after different intervals of exposure (2, 14, 20 and 35 days) at velocities of 18 m/s, 9 m/s, and 3 m/s, in order to determine the time required to achieve steady-state conditions with respect to corrosion rate and surface appearance. The panels exposed at 30, 15, 12 and 6 m/s were left undisturbed over the entire testing interval.

#### E. Data Acquisition

Data acquisition during the course of the study included electrochemical potential and polarization measurements, weight loss measurements, pit depth measurements, and profilometry measurements. In addition, the exposed panels were examined in detail using both an optical and a Scanning Electron Microscope.

Electrochemical data were obtained utilizing techniques which are adequately described in the literature. Weight loss data were obtained using an analytical balance accurate to  $\pm 0.5$  gm. A Clevite Surfanalyzer Model 21-1330-20 was used to monitor changes in surface roughness. The unit permits detection of surface variations as small as .03 microns.

Data was obtained daily on seawater samples from the channel including temperature, salinity, dissolved oxygen concentration, pH, turbidity, iron, and copper concentration. Table II presents the average seawater chemistry over the course of the study.

### III. RESULTS AND DISCUSSION

#### A. Corrosion Rate Versus Velocity

Figure 5 shows the change in corrosion rate versus velocity along with pictorial inserts showing the corresponding change in surface appearance for the 5456 aluminum alloy. The

corrosion rates were determined by weight loss after 35 days exposure (20 days exposure at 30 m/s). At high velocities, the surfaces appeared smooth and shiny while at the lower velocities the test panels were encrusted with a combination corrosion product/slime film. The observed changes in surface morphology are more fully discussed later in this report. The corrosion rate in quiescent seawater was 0.37 mdd and increased to about 6 mdd at the lowest channel velocity examined, 3 m/s. The corrosion rate was relatively constant over the velocity range of 3 to 9 m/s, then increased continuously to 83 mdd at 30 m/s. The sharp increase in corrosion rate at velocities above 9 m/s suggests the existence of a threshold or "breakaway" velocity similar to that observed by Efird<sup>2</sup> for copper-nickel alloys. Efird proposed that as increasing velocity causes a corresponding increase in hydrodynamic shear stress, a point is reached where the fluid shear stresses are sufficient to disrupt the protective oxide film. This point occurs at the so-called breakaway velocity and is characterized by a sharp increase in corrosion rate.

Most investigators<sup>3-11</sup> agree that the corrosion resistance of aluminum alloys derives from the formation of a protective duplex oxide film. The duplex film is made up of a thin amorphous barrier layer,  $\text{Al(OH)}_3$ , and a thicker hydrated outer layer. The exact composition of the outer layer depends on the nature of the corrosive environment, such as temperature and pH. In seawater, the outer layer is probably composed of mono-hydrate orthorhombic crystalline boehmite,  $\gamma - \text{Al}_2\text{O}_3 \cdot \text{H}_2\text{O}$  or tri-hydrate monoclinic bayerite,  $\beta - \text{Al}_2\text{O}_3 \cdot 3\text{H}_2\text{O}$ . Hydragillite,

with the same stoichiometric composition as bayerite, but with a different crystalline structure, is also possible. In a chloride environment such as seawater, the film may be locally disrupted by the formation of metastable complexes (e.g.  $\text{AlCl}_4^-$ ) and pitting subsequently occurs.

In general, the amorphous  $\text{Al(OH)}_3$  layer is fairly constant in thickness (about 10 $\text{\AA}$ ) and does not provide significant protection. The outer layer, or layers, vary in thickness depending on the nature of the environment and provide different degrees of protection. High rates of corrosion can occur on aluminum alloys by breakdown of the protective film, either locally via pitting or generally when the film becomes unstable. It is known that the protective film becomes unstable at both low and high pH. It now appears that the film becomes unstable at high velocity.

#### B. Corrosion Rate Versus Time

A series of panels were exposed at 18 m/s for various time periods and the corrosion rate determined by weight loss measurements. These tests were conducted in order to determine the time required to establish steady state conditions. Figure 6 shows the weight loss as a function of time on the 5456 aluminum alloy and Figure 7 shows the corresponding corrosion rates and surface appearance. The results indicate that a steady-state corrosion rate was achieved after two days at this velocity. However, it required closer to 20 days to achieve an apparent steady-state surface appearance. Based on these results, it appears

that steady-state corrosion rates are achieved very rapidly above the 9 m/s threshold velocity, while the characteristic surface appearance takes considerably longer to develop.

Attempts were made to determine the corrosion rate-time behavior below the 9 m/s threshold velocity. No weight loss was detectable after two days exposure at 6 m/s. Small weight losses could not practically be measured due to the large size of the test panels (about 2,100 grams) which required the use of a relatively insensitive balance having an accuracy of only  $\pm$  0.5 gm. It is assumed that steady state was achieved after 35 days of exposure below the threshold velocity.

#### C. Surface Morphology

The surfaces of the test panels were examined using both an optical and Scanning Electron microscope. Observations were made as a function of exposure time and seawater velocity. Results are presented after exposure periods of 2 days and 14 days for velocities of 3 m/s, 9 m/s and 18 m/s; after 35 days for velocities of 3 m/s, 6 m/s, 9 m/s, 12 m/s, 15 m/s and 18 m/s; and after 22 days at a velocity of 30 m/s.

##### 1. 2 Days Exposure at 3 m/s, 9 m/s and 18 m/s

Figure 8 shows the macroscopic appearance of test panel surfaces after 2 days exposure at 18 m/s (Figure 8a), 9 m/s (Figure 8b), and 3 m/s (Figure 8c). Figure 8d shows an unexposed

panel for comparison. All of the panels exhibited a mottled appearance after 2 days at velocity. Higher magnification micrographs (Figures 9a thru 9c) suggested that the hydrated oxide outer layer was being removed at the higher velocities, whereas at the lower velocity there appeared to be localized building or accumulation of corrosion products. Although different phenomena seemed to be occurring at higher versus lower velocities, the resulting macroscopic appearance was similar.

2. 14 Days Exposure at 3 m/s, 9 m/s and 18 m/s

Figures 10a thru 10c show the macroscopic appearance of test panels exposed at 3, 9 and 18 m/s. The test panels still exhibited a "mottled" appearance, which at higher magnification appeared as contrasting light and dark areas (Figure 11). The panel exposed at 3 m/s exhibited an accumulation of corrosion products in some areas with an apparently stable oxide film in the remaining areas. Small particles were barely visible on the panel exposed at 3 m/s. At 9 m/s, the small particles stood out in relief and at 18 m/s, the particles were even more evident. The particles were analyzed by EDX and appeared to be (Cr, Fe, Mn) Al<sub>6</sub> intermetallic compounds. These intermetallic particles are typical for the 5456 alloy. At 18 m/s, closer examination around the particles in the light areas showed crazing of the oxide layer downstream from the particles (Figure 12). Pitting occurred around the particles in dark areas, but crazing downstream of the particles was not observed.

In both areas, pitting was most intense in the areas immediately adjacent to the particles. This same sort of phenomena was apparent on the test panel exposed at 9 m/s, only to a lesser degree.

3. 35 Days Exposure at 3, 6, 9, 12, 15 and 18 m/s

A striking contrast in surface appearance as a function of velocity was apparent on the panels removed after 35 days. Figures 13 and 14 show the typical macroscopic and low magnification appearance of panels exposed at 6 different velocities. At 3 m/s, the panels were encrusted with an uneven layer of corrosion products with small mounds of corrosion product evident at random locations on the surface. Pits were present at these locations after removal of corrosion products. The maximum pit depth approached 266 microns, while the average pit depth was approximately 130 microns. The panels at 18 m/s exhibited a smooth, highly reflective, glossy surface with no detectable corrosion products. The pitting intensity decreased with increasing velocity. Above 9 m/s, the visual corrosion attack appeared to have occurred uniformly, although subsequent high magnification examination would show micropitting at intermetallic particles. Table I presents the results of glossmeter measurements on the surface and confirms quantitatively the observed changes.

Higher magnification inspection of the panels showed a diminishing oxide layer with increasing velocity (Figures

15 thru 19). The contrasting light and dark areas, clearly evident on the panel at 18 m/s after 14 days, were just barely detectable at the same velocity after 35 days. These contrasting areas are proposed to be associated with the presence or lack of presence of different oxide layers. Contrasting light and dark areas were strongly evident on the panel at 15 m/s. As velocity decreased, the panels evidenced an increasingly rougher profile and a heavier oxide scale.

The protuberance of intermetallic particles at 18 m/s was even more pronounced after 35 days than observed after 14 days. Again, at lower velocities, the intermetallic particles were obscured by the heavy oxide layer. Crazing of the oxide layer and pitting downstream of the particles was also more pronounced. Figure 20 presents a high magnification stereo micrograph\* showing quite clearly this preferred attack downstream of the intermetallic particles. While macroscopic inspection might suggest corrosion is occurring very uniformly at high velocity, microscopically, pitting corrosion is occurring preferentially around intermetallic particles especially downstream.

#### 4. 22 Days at 30 m/s

Macroscopically, the 5456 aluminum alloy exposed at 30 m/s for 22 days exhibited a highly reflective, apparently smooth surface much the same as reported for the panels exposed at 18 m/s for 35 days. However, higher magnification examination (Figures 21 thru 24) disclosed denser micropitting than had been

\*A stereo viewer is attached to the back cover of this report for the reader's convenience.

observed at 18 m/s. The micropitting again initiated at intermetallic particle sites. Larger isolated pits  $\approx$  100 x the area of the smaller pits were also found. Pits of this size were not observed at 18 m/s. The average depth of these larger pits was  $\approx$  30 microns as compared to  $< 5$  microns for the smaller pits. The density of the larger pits was approximately 2 pits/cm<sup>2</sup> versus 800/mm<sup>2</sup> for the smaller pits.

Higher magnification SEM examination also revealed that the intermetallic particles, while visible, were no longer standing out in relief. For the most part, the visible intermetallic particles were sitting down in pits and not protruding above the surface plane. There appeared to be many more empty pits elongated in the direction of flow that had once been occupied by intermetallic particles. The lack of protruding intermetallic particles is opposite to what was seen at 18 m/s. This suggests that the fluid shear stresses are of sufficient magnitude to cause the particles to be "ripped" from the matrix when the least bit of particle protrudes into the flow stream. Figures 25 thru 31 present stereo-pair micrographs which enable the reader to see 3-D images and better visualize this reported corrosion behavior.

##### 5. Profilometry Measurements

Although the test panels exposed at high velocity appeared to be much smoother and more reflective than unexposed control panels, profilometer measurements established that the surface roughness had increased slightly as compared to an un-

exposed control panel. Figures 32 and 33 show the profile trace for both an unexposed panel and a panel exposed for 35 days at 18 m/sec. Thus, the measured increase in gloss at high velocity cannot be ascribed to a polishing effect since the as-exposed surface is rougher than the initial control surface.

The increase in surface gloss is probably indicative of a change in the reflective characteristics of the surface films. Ellipsometry studies<sup>1,2</sup> have shown that the refractive index varies for different oxides formed on aluminum alloys. The results of the SEM surface examination clearly point to different degrees of oxide removal/formation dependent on velocity. The profilometry data which shows that changes in surface roughness cannot account for the observed increase in reflectivity offers additional circumstantial evidence.

D. Corrosion Potential and Polarization Resistance  
Versus Velocity

Figure 34 presents the average corrosion potential measured at each velocity over the 35 day test period. The corrosion potential exhibited a slight shift toward more active values as velocity increased. This is not surprising considering the results of the surface examination. A reduction in the thickness in the protective oxide layer would be expected to increase the diffusion-limited current density. If the cathodic polarization curve is unaffected by increases in velocity, the corrosion potential would be predicted to shift in the active direction as shown on a polarization diagram in Figure 35.

Polarization resistance measurements were made throughout the 35 day test run. Corrosion rates were calculated from the polarization resistance measurements using the Stearn-Geary technique<sup>13</sup> as later modified by Mansfeld<sup>14</sup>. Tafel constants ( $\beta_a$  &  $\beta_c$ ) were calculated according to the curve-fitting method suggested by Mansfeld<sup>14</sup> because full anodic and cathodic polarization curves did not yield unambiguous Tafel slopes. The approximate Tafel constants calculated from the polarization resistance curves were  $\beta_a = .120$  and  $\beta_c = .120$ . The shape of the polarization resistance curve did not change significantly as a function of velocity and therefore,  $\beta_a = .120$  and  $\beta_c = .120$  were used throughout all of the corrosion rate calculations.

Figure 36 presents the average corrosion rate calculated at each velocity over the 35 day test period. Corrosion rates determined by weight loss as previously shown in Figure 1 are shown again for reference. At lower velocities (3 m/s to 9 m/s) the data are within the expected accuracy limits generally associated with the polarization resistance method. However, at higher velocities, there is a considerable difference. The same order-of-magnitude difference was observed in previous work by Davis and Gehring<sup>15</sup>.

Consideration of the criteria necessary for valid application of the polarization resistance technique does not provide a clear-cut answer why such a large difference should exist. The polarization response to a current step observed on an oscilloscope indicated that ohmic voltage drops were not present and thus could not account for the error. It is possible

that concentration polarization is present, however, the possible degree of error associated with concentration polarization effects ( $\beta_a = \infty$  or  $\beta_c = \infty$ ) doesn't appear sufficient to account for the observed difference. It is also possible that the equilibrium potential for the reduction reaction is too close to the corrosion potential. However, the error arising from the close proximity of the half-cell redox potential to the corrosion potential results in predicted corrosion rates that are higher than those determined by weight loss as shown by Mansfeld and Oldham<sup>16</sup>. This is opposite to what was obtained. In the same respect, the difference doesn't appear attributable to a secondary reaction effect.

The possibility was also considered that the difference reflects weight loss associated with purely hydromechanical wear not detectable by the polarization resistance technique. While there was certainly evidence of intermetallic particle removal by purely hydromechanical forces, there was no evidence of selective grain boundary attack which could result in whole grain dropping. The hydromechanical removal of intermetallic particles can't account for the difference. Furthermore, the possibility of removing base metal by hydromechanical wear is discounted because of other as-yet unpublished work conducted by this author where solvent-type coating materials exhibited negligible weight loss under identical exposure conditions. The cohesive strength of the coating materials is certainly less than the cohesive strength of the 5456 alloy. Thus, the reason for the observed difference, remains uncertain.

## E. Limiting Oxygen Diffusion Current Versus Velocity

Numerous authors have suggested that the rate of mass transfer of dissolved oxygen to the corroding surface is often the rate-determining step in high velocity seawater corrosion.<sup>17-22</sup> Furthermore, equations relating limiting oxygen diffusion current to velocity were derived, most notably by Levich<sup>22</sup>. However, experimental verification of these equations has not been convincing, especially under high velocity, turbulent conditions. Based on a review of this work, it was proposed by Davis and Gehring<sup>1</sup> that the limiting diffusion current density for oxygen should be proportional to the velocity to the one-fifth power for turbulent conditions or to the one-half power for laminar conditions as follows:

$$(1) \quad i_L = \frac{Dn F C_B}{\delta_m} \quad (\text{from Fontana \& Greene}^{23})$$

$$(2) \quad Re = \frac{VL}{D}$$

$$(3) \quad \delta_h = L(30/Re)^{.5} \quad (\text{from Rohsenow \& Choi}^{24} \text{ for laminar conditions})$$

$$(4) \quad \delta_h = .37 L (Re)^{-1.2} \quad (\text{from Rohsenow \& Choi for turbulent conditions})$$

$$(5) \quad \delta_m = \frac{\delta_h}{Sc^{1/3}} \quad (\text{from Levich})$$

$$(6) \quad Sc = \frac{V}{D}$$

where,

$i_L$  = limiting oxygen diffusion current density

$D$  = diffusion coefficient for oxygen

$n$  = number of electrons transferred

$F$  = Faraday's constant

$C_B$  = bulk solution concentration of oxygen

$\delta_m$  = mass transport boundary layer thickness

Re = Reynolds Number

V = velocity

L = equivalent length

$\nu$  = kinematic viscosity

$\delta_h$  = hydrodynamic boundary layer

Sc = Schmidt Number

By substitution and elimination, these equations reduce to:

$$i_L = \frac{D^{.67} n F C_B V^{.5}}{5.48 L^{.5} \nu^{.17}} \quad \text{for laminar flow}$$

and,

$$i_L = \frac{D^{.67} n F C_B \nu^{.12} V^{.2}}{.38 L^{.8}} \quad \text{for turbulent flow}$$

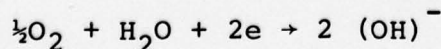
If all variables are maintained constant except for velocity,

$$i_L \propto V^{.5} \quad \text{for laminar flow}$$

and,

$$i_L \propto V^{.2} \quad \text{for turbulent flow}$$

Cathodic polarization measurements were made on platinum electrodes in quiescent seawater and over a range of seawater velocities. The results of these measurements are shown in Figure 37. The limiting diffusion current density in quiescent seawater was about  $50 \mu\text{A}/\text{cm}^2$ , in reasonable agreement with the literature<sup>23</sup> for the following reaction:



A limiting diffusion current density was not observed at any of the seawater velocities. The polarization curves show apparent Tafel behavior, however, the calculated Tafel constants ( $\beta_c \approx .3$  v/decade) appear too large for strict charge transfer or activation control. It is believed that the cathodic polarization curves reflect mixed control (both charge transfer and mass transfer). The lack of experimental verification suggests the derived equations are not applicable under the high velocity, turbulent flow conditions characteristic of the subject study.

F. Comparison of Flow Channel and Water Wheel Results

Figure 38 compares corrosion rates determined as a function of velocity in the subject study versus corrosion rates determined in previous work using a water wheel. Corrosion rates determined in the water wheel were higher on the 5456 aluminum alloy compared to corrosion rates determined in the flow channel at velocities greater than 3 m/s. Although there was a significant difference in relative magnitude, the shape of the corrosion rate versus velocity plots was similar. It is believed that the higher corrosion rate observed on specimens exposed in the water wheel is attributable to greater corrosion on the leading edge. The specimens exposed in the water wheel were subject to impingement-type flow on the leading edge. Panels exposed in the flow channel were subjected to parallel flow, only.

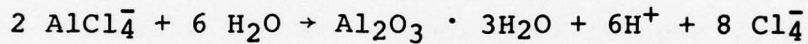
Figure 39 compares corrosion potentials as a function of velocity in the water wheel versus the flow channel. The corrosion potential determined in the water wheel was consistently more active than corrosion potentials determined in the flow channel. The leading edge corrosion observed on specimens exposed in the water wheel could account for the more active corrosion potential. Impinging flow at the leading edge causing hydro-mechanical removal of the protective oxide film and greater exposure of unprotected aluminum could result in a more active corrosion potential.

#### G. Summary

The morphological changes observed as a function of velocity clearly suggest that the nature and stability of the protective oxide layer is velocity-dependent; and, that the removal or disruption of the oxide film is a primary factor affecting both the mode and rate of corrosion. Below 9 m/s where the oxide layer is fairly stable, corrosion appears to proceed in the classical manner generally acknowledged for aluminum alloys in seawater. Above 9 m/s, however, the oxide layer (or layers) becomes unstable and corrosion increases sharply while changing from a macropitting mode to a micropitting mode.

The micropitting mode comes into play because the elimination of the oxide diffusion barrier allows the intermetallic particles to exert a much stronger influence. Pitting corrosion initiates at the intermetallic particles, probably

because the film is less protective at these points and because of the galvanic action between the aluminum matrix and more noble intermetallic particles. At the same time, general metal loss on the surface causes the intermetallic particle to protrude into the flow stream. Up until this point, pitting occurs uniformly about the intermetallic particle. However, with the intermetallic particle protruding increasingly into the flow stream, pitting begins to break-out and occur much more rapidly downstream of the particle. This occurs because of the localized increase in turbulence immediately downstream of the particle and possibly, due to a localized pH effect. The pH effect could occur as the result of the hydrolysis of metastable  $\text{AlCl}_4^-$  hypothesized by Becerra and Darby<sup>3</sup> as follows:



The  $\text{H}^+$  ions could then be swept downstream causing a localized drop in pH and subsequent dissolution of the oxide film. Eventually, the intermetallic particle is undermined and removed by hydrodynamic shear stresses. Once the intermetallic particle is gone, the galvanic cell no longer exists and the rate of pitting corrosion decreases. Flow stagnation in the remaining depression results in a corrosion rate lower than the rest of the surface. This process, repeated over and over, results in a relatively uniform metal loss which, macroscopically, gives a very smooth surface appearance. Figure 40 illustrates this behavior in stepwise fashion.

#### IV. CONCLUSIONS

1. The corrosion rate of 5456-H117 aluminum is velocity dependent and increases sharply with increasing velocity above 9 m/s.
2. The protective oxide film(s) which characteristically forms on 5456-H117 aluminum begins to breakdown at velocities above 9 m/s.
3. The basic mechanism for high velocity corrosion of 5456-H117 aluminum involves film disruption/removal leading to enhanced micropitting about intermetallic particles.
4. The corrosion rate reaches steady-state within a few days at high seawater velocities (> 9 m/s).
5. The surface appearance characteristic of each velocity takes considerably longer time to reach steady-state ( $\approx$  20 days).
6. Corrosion changes from a macropitting mode to a micro-pitting mode with increasing velocity. Macroscopically, corrosion occurs uniformly at high velocities.
7. The transport of dissolved oxygen to a corroding surface is not strictly diffusion-limited under the high Re flow conditions characteristic of this study.

8. Impingement-type flow can cause significantly greater corrosion rates as compared to parallel flow.

V. REFERENCES

1. J. A. Davis and G. A. Gehring, "Pitting Behavior of Aluminum Alloys In High Velocity Seawater", a paper presented at the Annual Conference of the Electrochemical Society, October, 1976
2. K. D. Efird, Corrosion, Vol. 33, No. 1, January, (1977)
3. A. Becerra & R. Darby, Corrosion, Vol. 30, No. 5, May (1974)
4. M.S. Hunter & P. Fowler, Jnl. Elec. Chem. Soc., Vol. 103, No. 9, September, (1956)
5. J.E. Draley & W.E. Ruther, Corrosion, Vol. 12, (1956)
6. A.C. Fraker & A.W. Ruff, Corrosion, Vol. 27, No. 4, April (1971)
7. V.H. Troutner, Corrosion, Vol. 15, (1959)
8. D.F. MacLennan, Corrosion, Vol. 17, April, (1961)
9. D.F. MacLennan, Corrosion, Vol. 17, May, (1961)
10. R.L. Dillon, Corrosion, Vol. 15, January, (1959)
11. M.J. Dignam, Jnl. Elec. Chem. Soc., Vol. 109, No. 3, March, (1962)
12. J. Kruger & P.C.S. Hayfield, Handbook On Corrosion Testing and Evaluation, J. Wiley & Son, New York, 1971
13. M. Stern & A.L. Geary, Jnl. Elec. Chem. Soc., Vol. 104, No. 56, (1957)
14. F. Mansfeld, Corrosion, Vol. 29, No. 10, October, (1973)
15. J.A. Davis and G.A. Gehring, Materials Performance, Vol. 14, No. 4, April, (1975)
16. F. Mansfeld & K.B. Oldham, Corrosion Science, Vol. 11, (1971)
17. B.C. Syrett, Corrosion, Vol. 32, No. 6, June, (1976)
18. F. Mansfeld and J. V. Kenkel, Corrosion, Vol. 33, No. 10, October, (1977)
19. J. Perkins, et.al., "A Study of the Effect of Velocity on Corrosion of Galvanic Couples in Seawater Using a Circling-Foil Apparatus", a paper presented at the NACE Conference, Houston, March, 1978

20. I. Cornet, R. Greif, and F. Roehler, "Mass Transfer Controlled Corrosion/Polarization of Prototype Impellers/Propellers", a paper presented at the AIChE Annual Meeting, New York, November, 1977
21. J.T. Kim and J. Jorne, "Mass Transfer and Electrochemical Kinetics Studies of Corrosion", a paper presented at the AIChE Annual Meeting, New York, November, 1977
22. V.G. Levich, Physicochemical Hydrodynamics, Prentice-Hall, Englewood Cliffs, 1962
23. M.G. Fontana and N.D. Greene, Corrosion Engineering, McGraw-Hill, New York, 1967
24. W.M. Rohsenow and H. Choi, Heat, Mass and Momentum Transfer, Prentice-Hall, Englewood Cliffs, 1961

TABLE 1 - TYPICAL COMPOSITION OF 5456-H117 ALUMINUM

wt, %

Al	Mg	Mn	Cr	Cu	Zn	Ti	Si+Fe	Other
Bal	4.7-5.5	.50-1.0	.05-.20	.10 max.	.25 max.	.20 max.	.40 max.	.15 max.

TABLE II - SEAWATER CHEMISTRY DURING VELOCITY STUDIES

	<u>MAXIMUM</u>	<u>MINIMUM</u>	<u>AVERAGE</u>
Salinity, ppm	33,900	27,000	31,800
pH	8.1	7.8	7.9
Temperature, °C	22	19	20
Dissolved Oxygen, ppm	7.5	6.4	7.0
Turbidity, J.T.U.	10	1	2
Iron, ppm	.05	<.02	<.02
Cu, ppm	<.01	<.01	<.01

TABLE III - RESULTS OF GLOSS MEASUREMENTS\* ON TEST  
PANELS AFTER 35 DAYS AT VELOCITY

<u>VELOCITY</u>	<u>60° SPECULAR GLOSS</u>
18 m/s	>100
15 m/s	39
12 m/s	37
9 m/s	37
6 m/s	5
3 m/s	3
unexposed control	37

\*Measurements were made using a Gardener Glossmeter

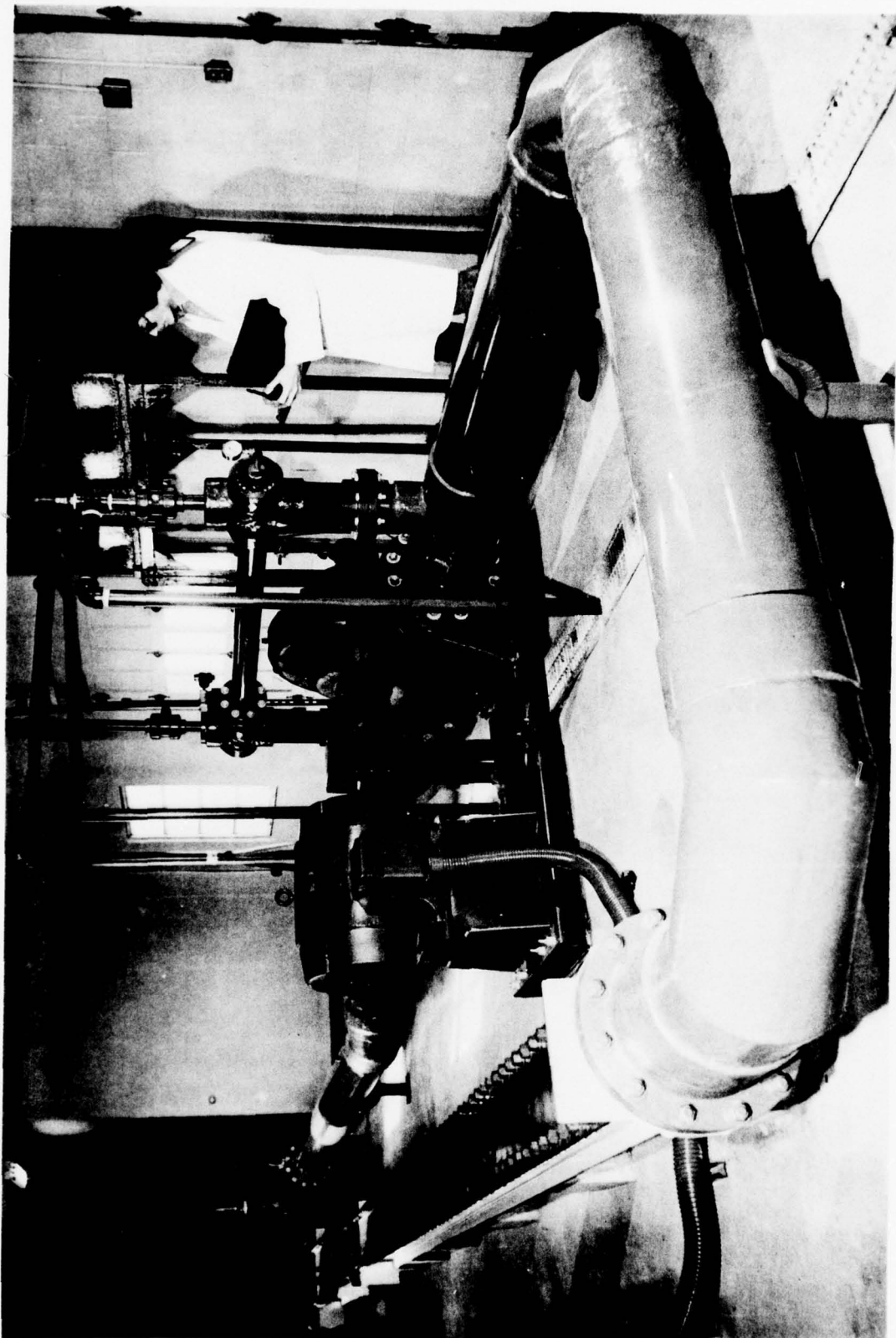


Figure 1  
High Velocity Flow Channel

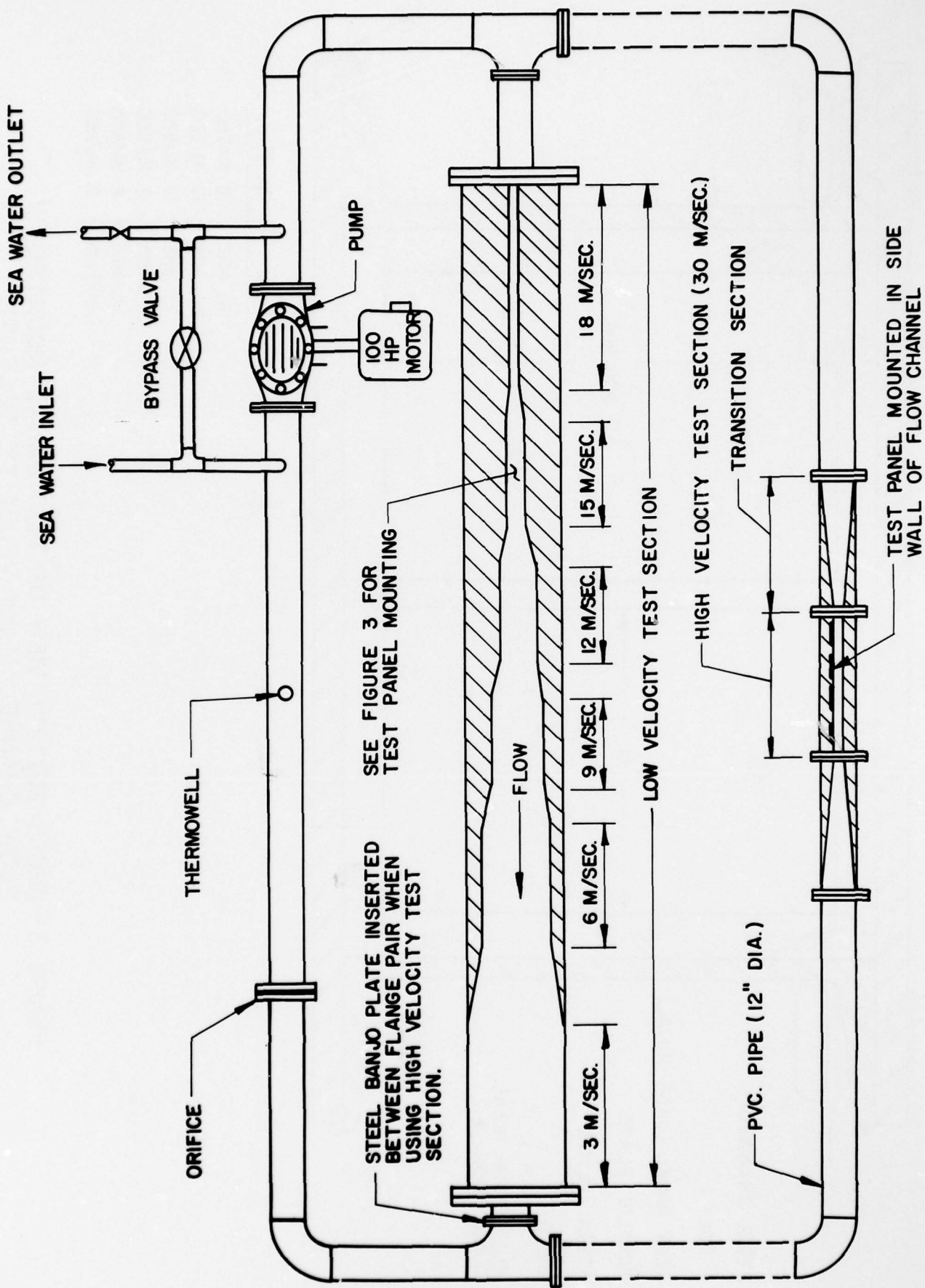


FIGURE 2—SIMPLIFIED SCHEMATIC OF FLOW CHANNEL

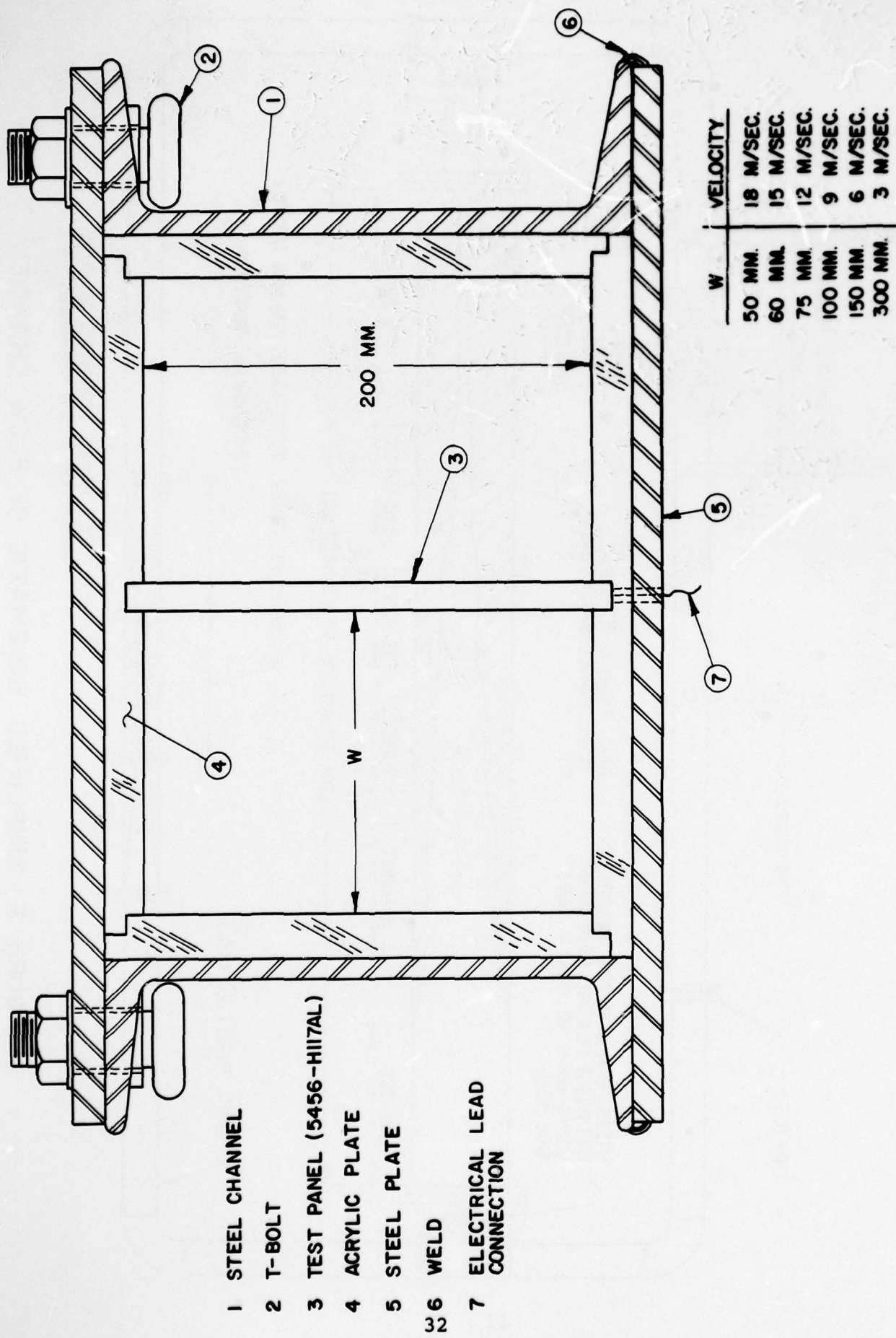


FIGURE 3 - CROSS-SECTION VIEW OF TEST PANEL MOUNTED IN FLOW CHANNEL (LOW VELOCITY SECTION)

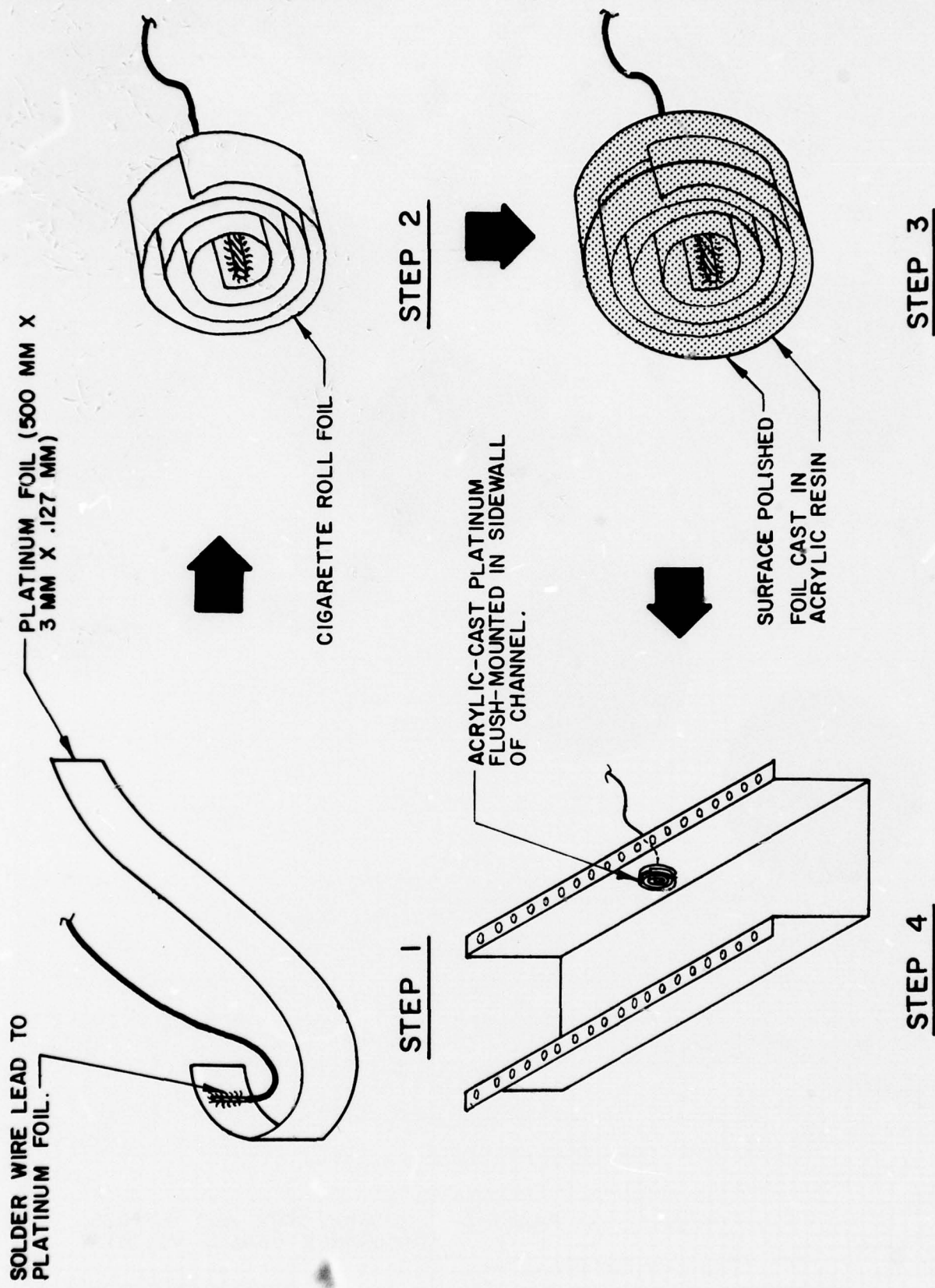


FIGURE 4 -PREPARATION AND MOUNTING OF PLATINUM ELECTRODES

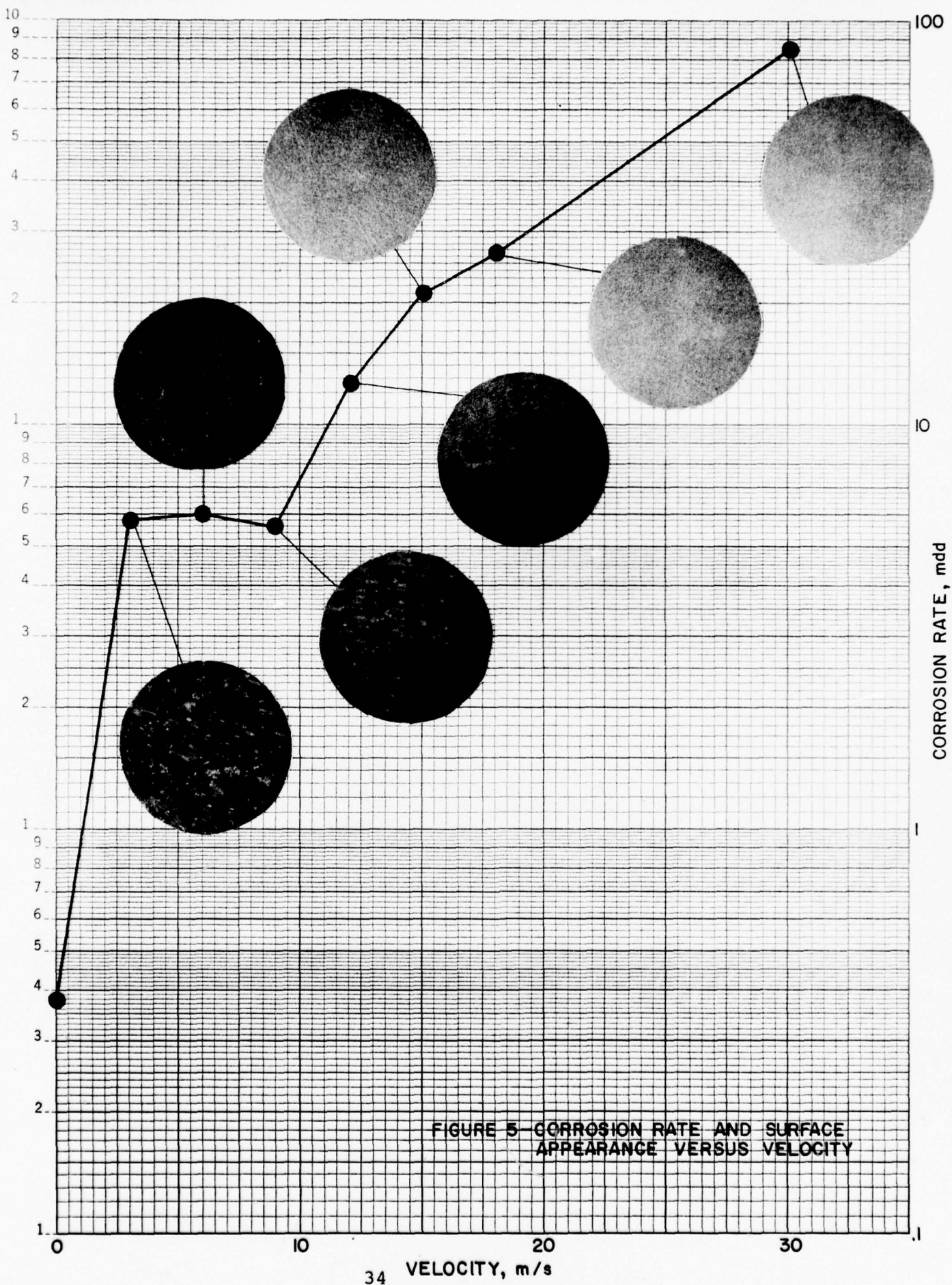


FIGURE 5-CORROSION RATE AND SURFACE APPEARANCE VERSUS VELOCITY

FIGURE 6-WEIGHT LOSS VERSUS TIME AT 18 MAS

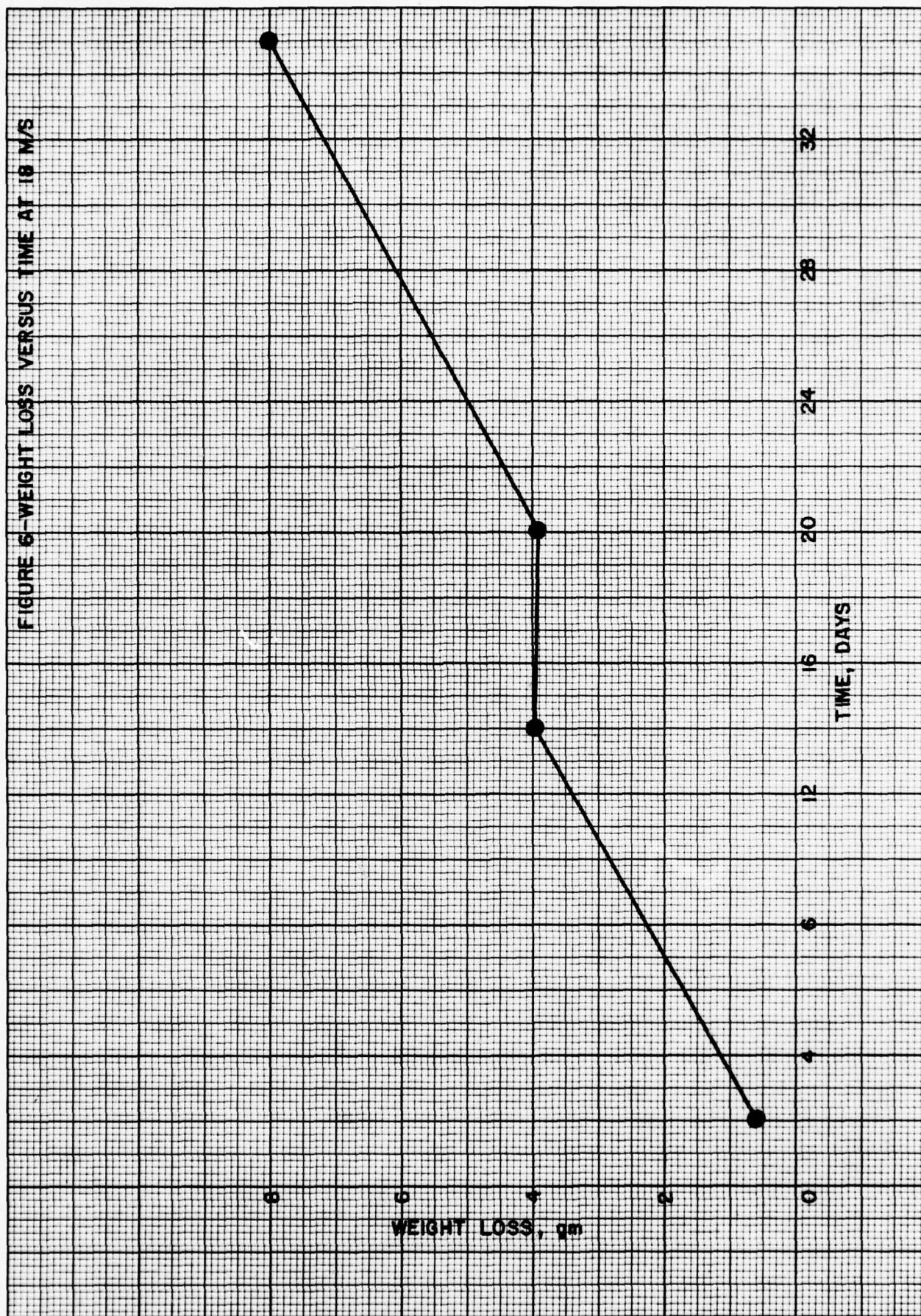
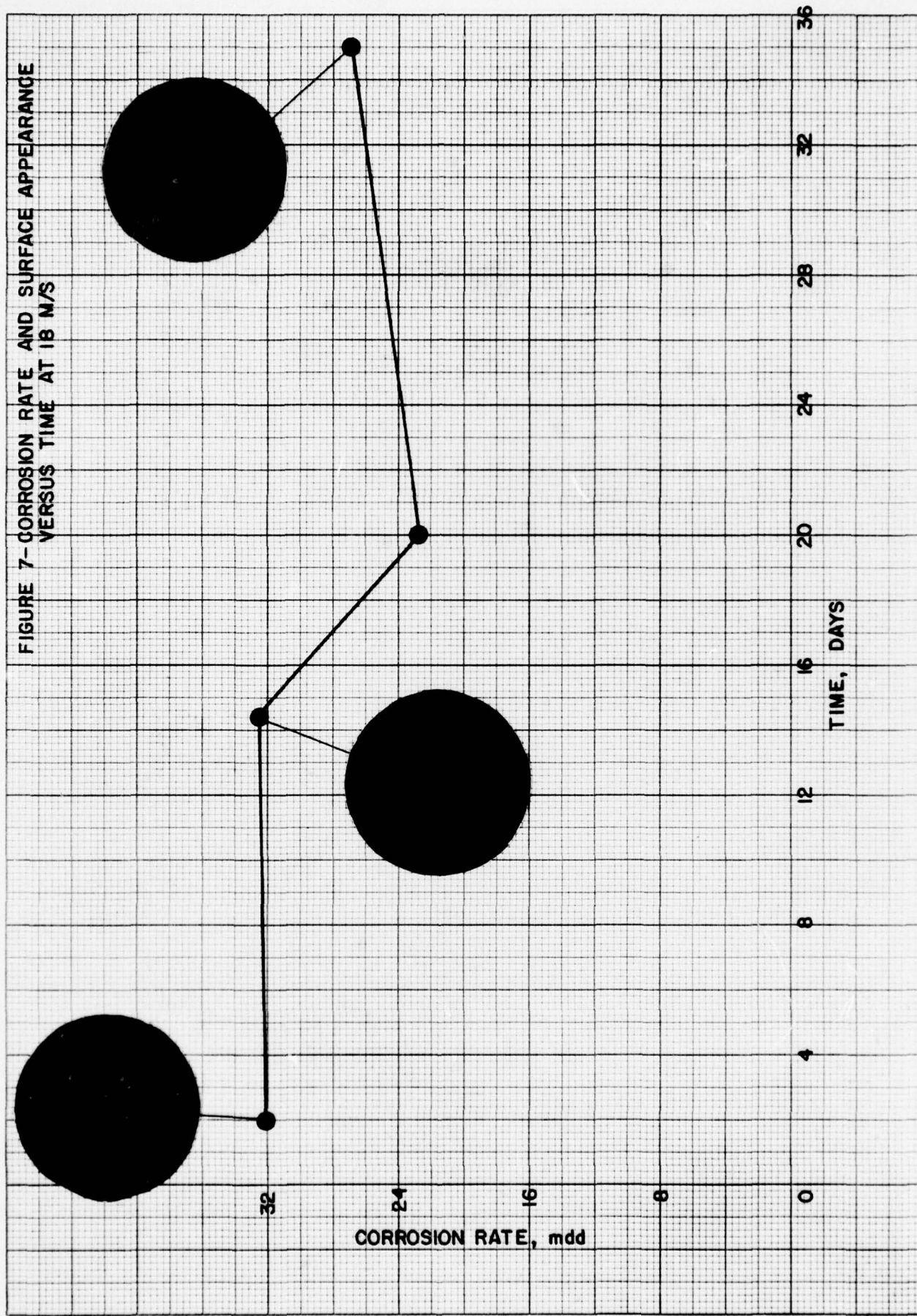


FIGURE 7-CORROSION RATE AND SURFACE APPEARANCE  
VERSUS TIME AT 18 N/S



Flow →

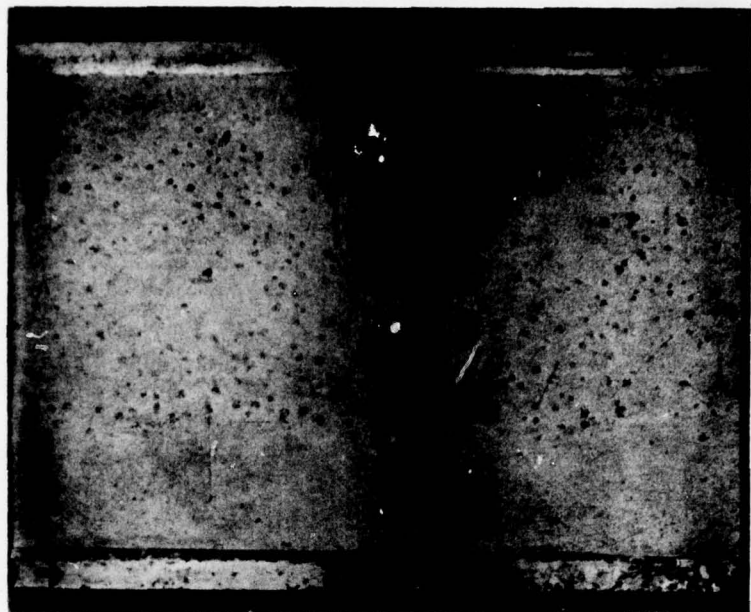


Figure 8a - Macroscopic Appearance of Test Panel After 2 Days Exposure at 18 m/s

Flow →

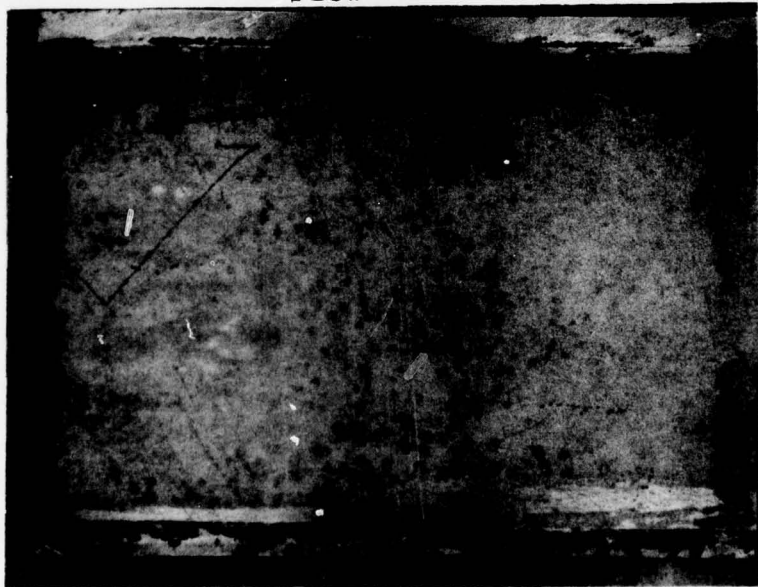
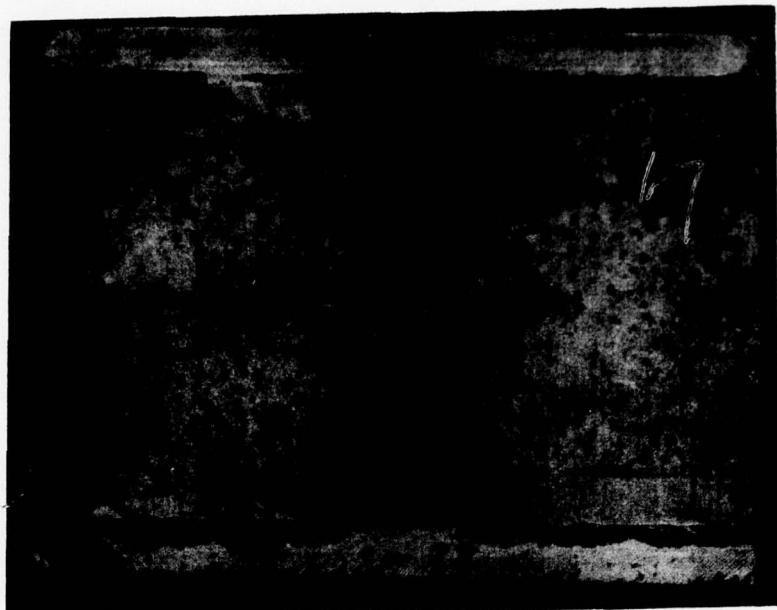
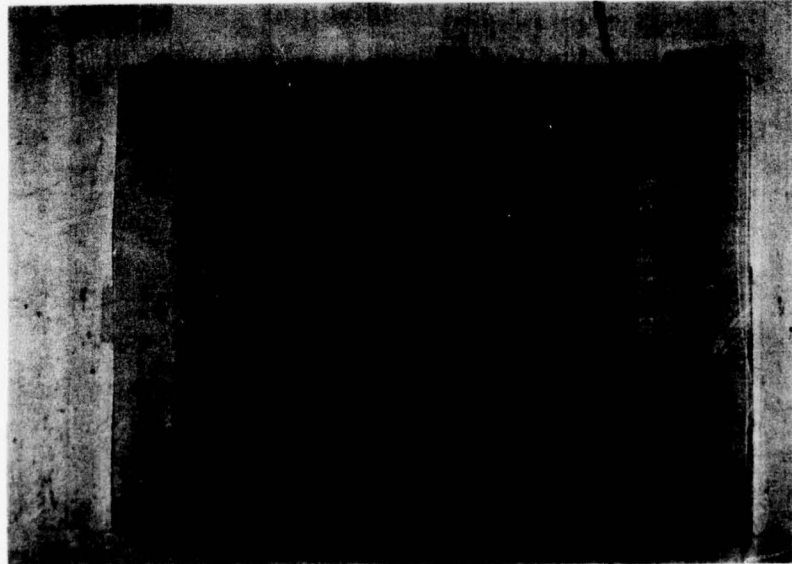


Figure 8b - Macroscopic Appearance of Test Panel After 2 Days Exposure at 9 m/s

Flow →



**Figure 8c - Macroscopic Appearance of Test Panel After 2 Days Exposure at 3 m/s**



**Figure 8d - Macroscopic Appearance of Unexposed Test Panel**

Flow →

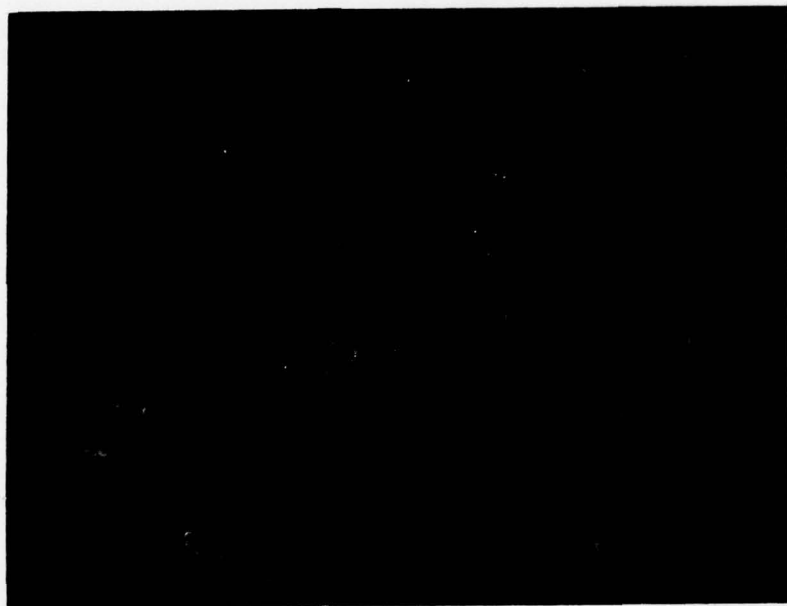


**Figure 9a - Low Magnification (4.5x)  
Appearance of Test Panel After 2 Days  
Exposure at 18 m/s**

Flow →



**Figure 9b - Low Magnification (4.5x)  
Appearance of Test Panel After 2 Days  
Exposure at 9 m/s**

Flow →



Figure 9c - Low Magnification (4.5x)  
Appearance of Test Panel After 2 Days  
Exposure at 3 m/s



Figure 9d - Low Magnification (4.5x)  
Appearance of Unexposed Test Panel

Flow +

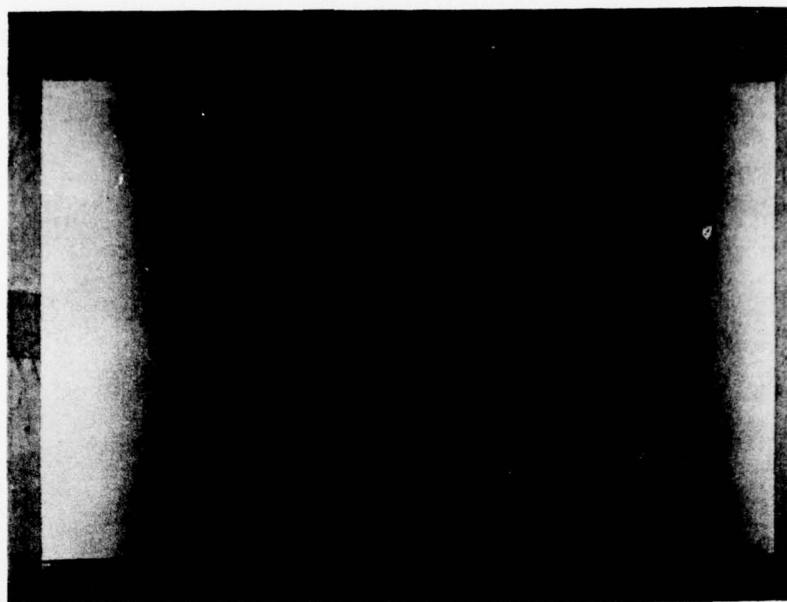


Figure 10a - Macroscopic Appearance of Test Panel After 14 Days Exposure at 18 m/s

Flow +

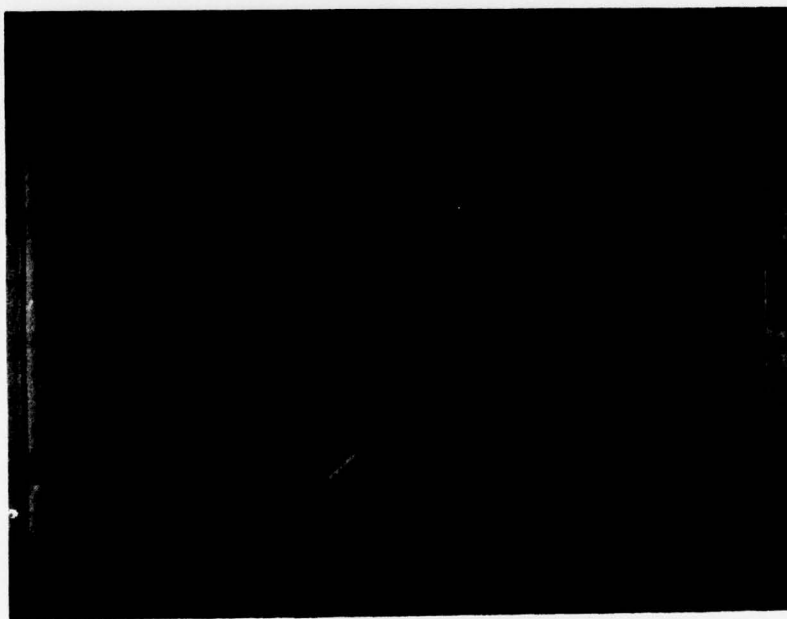


Figure 10b - Macroscopic Appearance of Test Panel After 14 Days Exposure at 9 m/s

Flow →

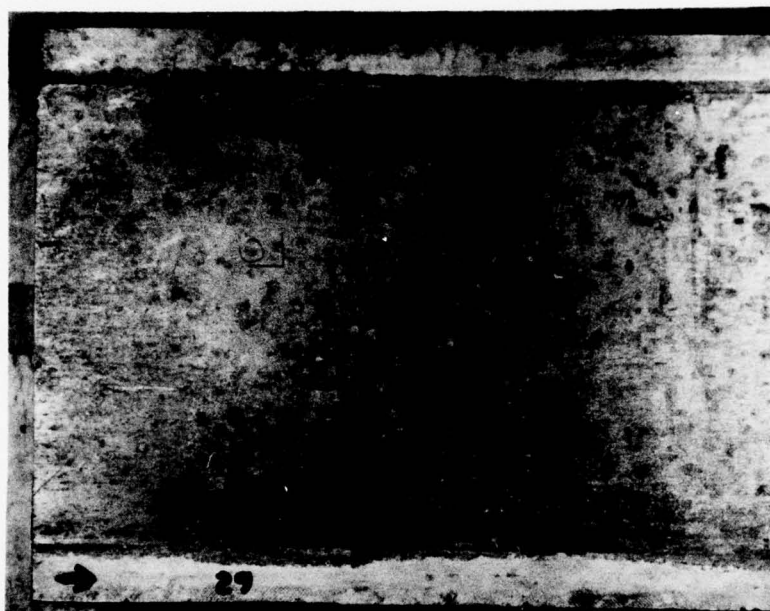


Figure 10c - Macroscopic Appearance of Test Panel After 14 Days Exposure at 3 m/s

Flow →



Figure 11a - Low Magnification (4.5x) Appearance of Test Panel After 14 Days Exposure at 18 m/s

Flow →



Figure 11b - SEM Micrograph of Test Panel After 14 Days Exposure at 18 m/s (55x)



**Figure 12a - SEM Micrograph Showing Crazing of  
Oxide Layer Downstream of Intermetallic  
Particles - 14 Days at 18 m/s (1000x)**



Figure 12b - SEM Micrograph Showing Crazing of  
Oxide Layer Downstream of Intermetallic  
Particle - 14 Days at 18 m/s (1000x)

Flow →

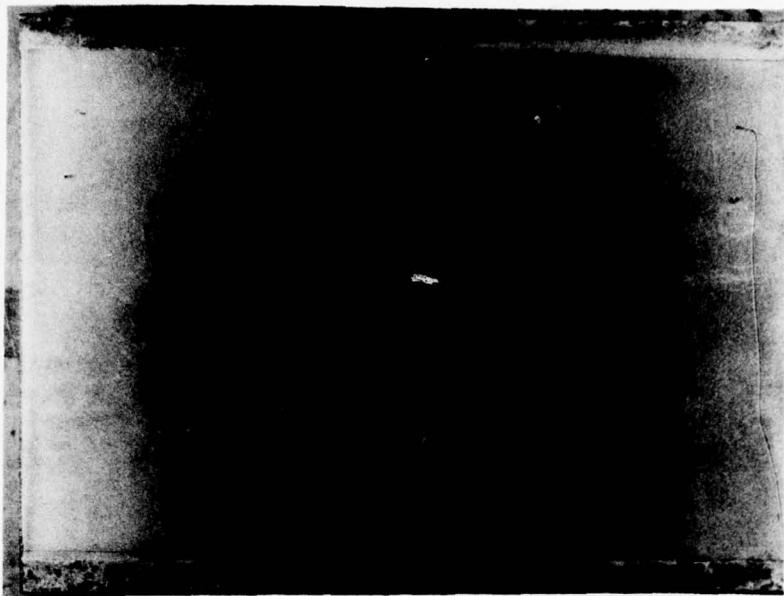


Figure 13a - Macroscopic Appearance of Test Panel After 35 Days Exposure at 18 m/s

Flow →

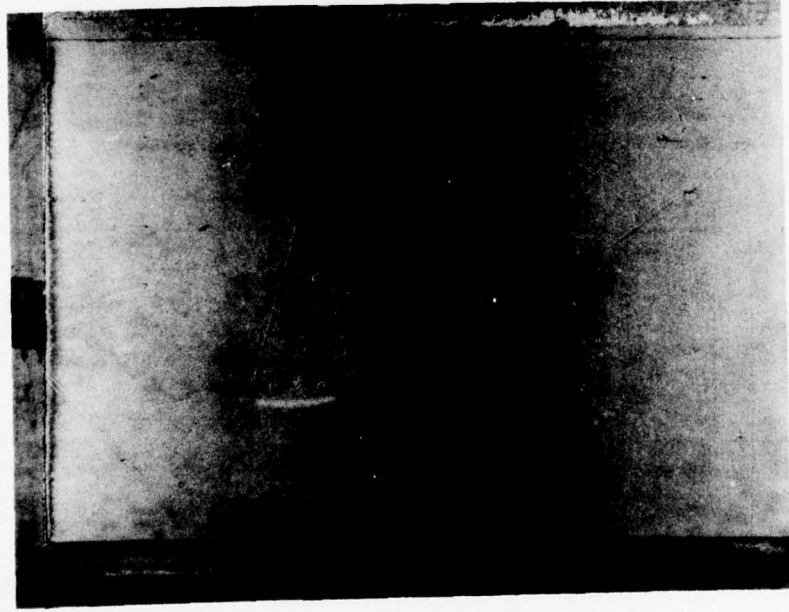


Figure 13b - Macroscopic Appearance of Test Panel After 35 Days Exposure at 15 m/s

Flow →

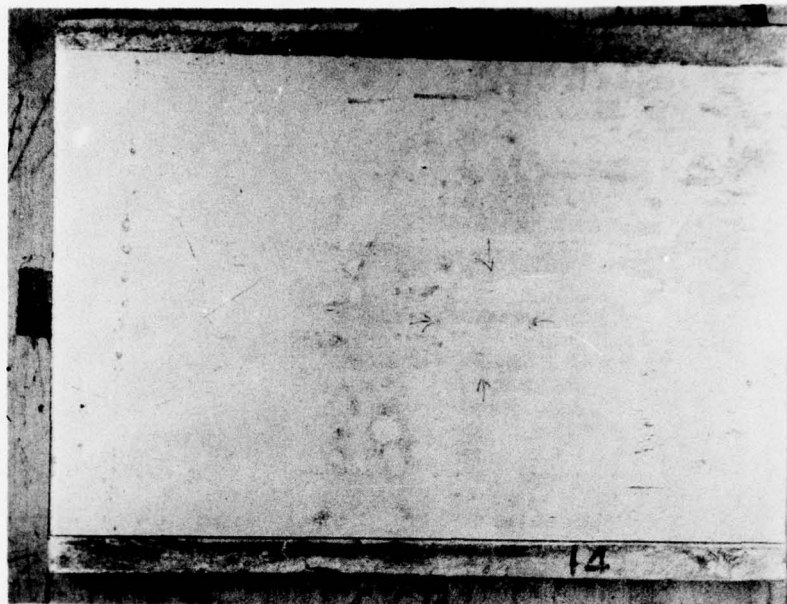


Figure 13c - Macroscopic Appearance of Test Panel After 35 Days Exposure at 12 m/s

Flow →

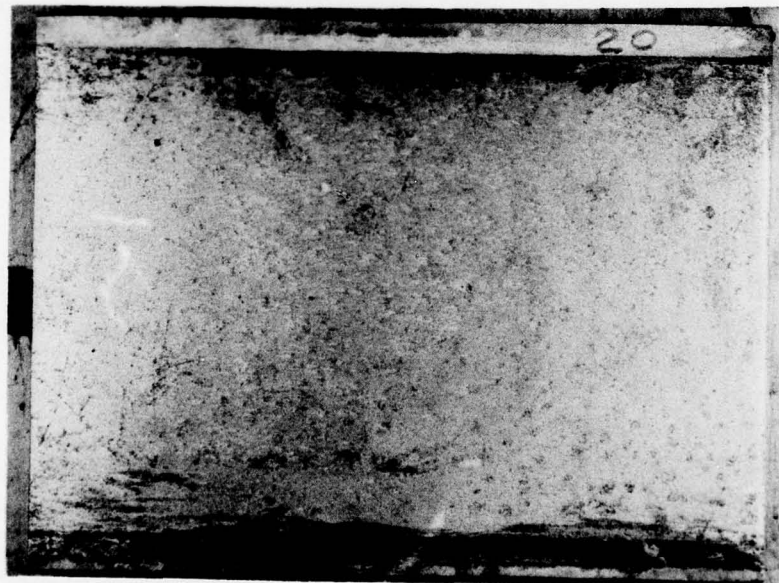


Figure 13d - Macroscopic Appearance of Test Panel After 35 Days Exposure at 9 m/s

Flow →

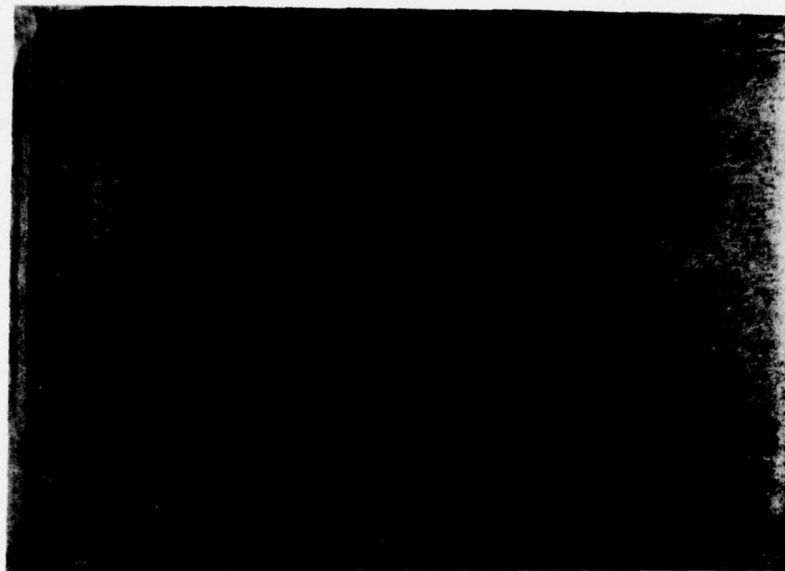


Figure 13e - Macroscopic Appearance of Test Panel After 35 Days Exposure at 6 m/s

Flow →

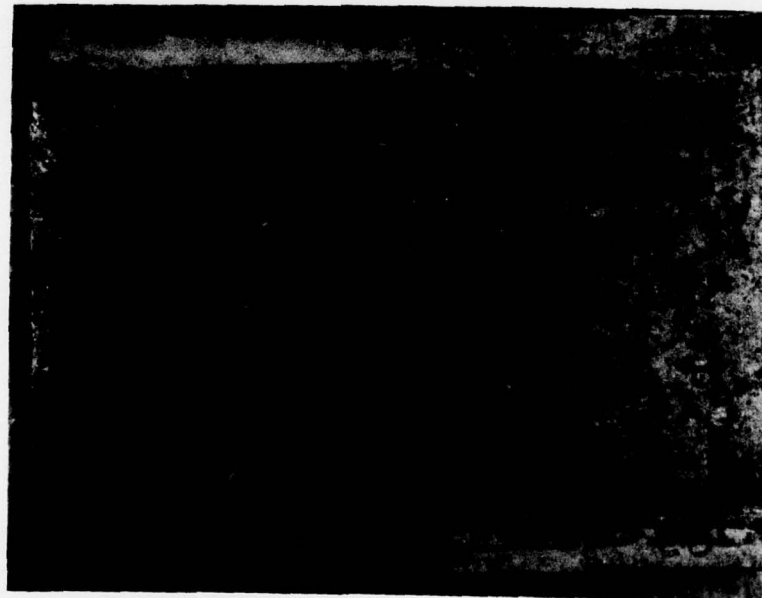


Figure 13f - Macroscopic Appearance of Test Panel After 35 Days Exposure at 3 m/s

Flow →

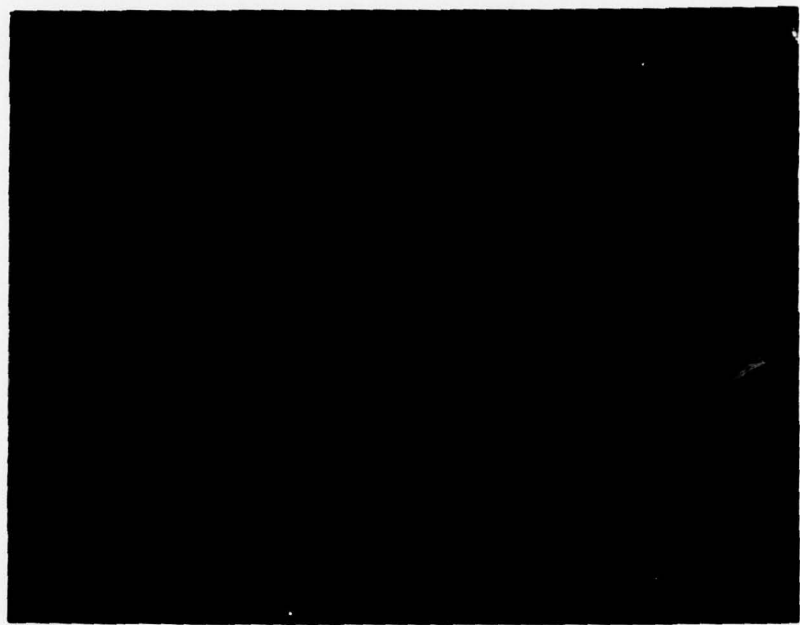


Figure 14a - Low Magnification (4.5x) Appearance of Test Panel After 35 Days Exposure at 18 m/s

Flow →

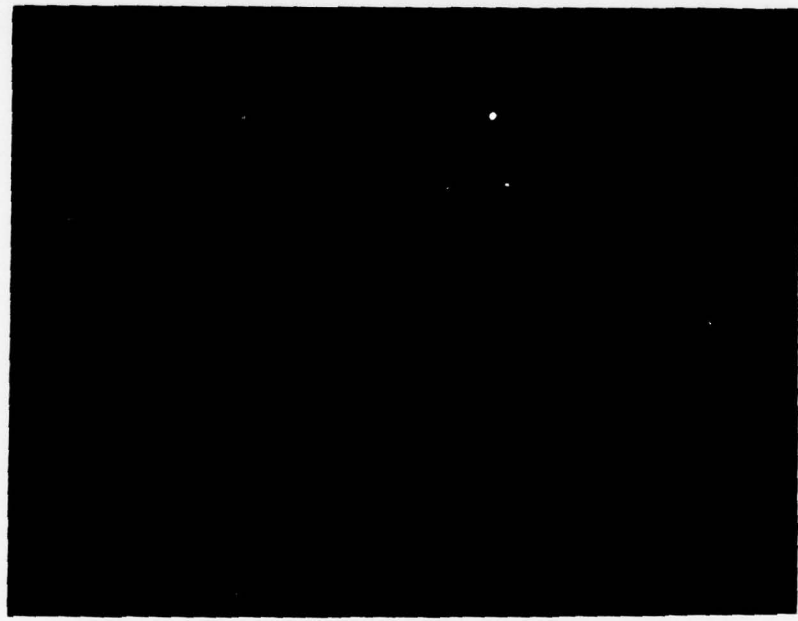


Figure 14b - Low Magnification (4.5x) Appearance of Test Panel After 35 Days Exposure at 15 m/s

Flow →

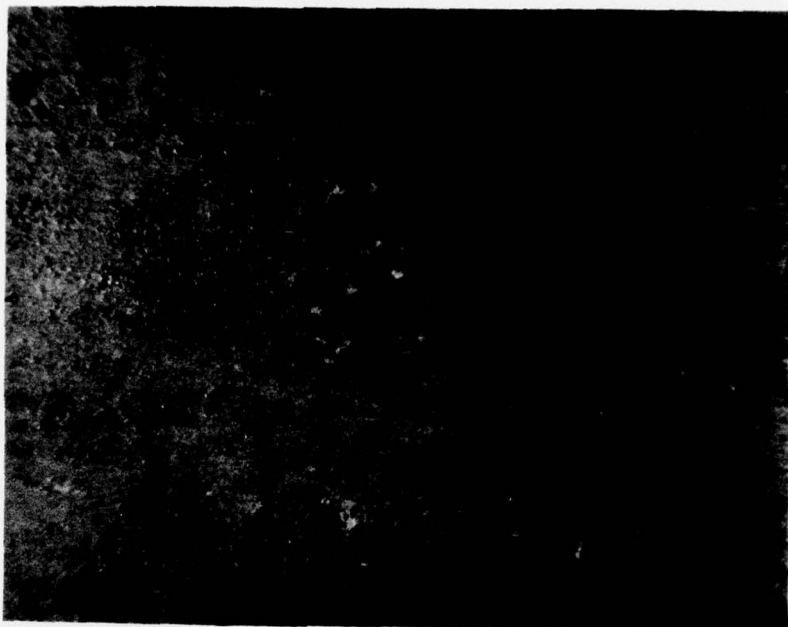


Figure 14c - Low Magnification (4.5x) Appearance of  
Test Panel After 35 Days Exposure at 12 m/s

Flow →

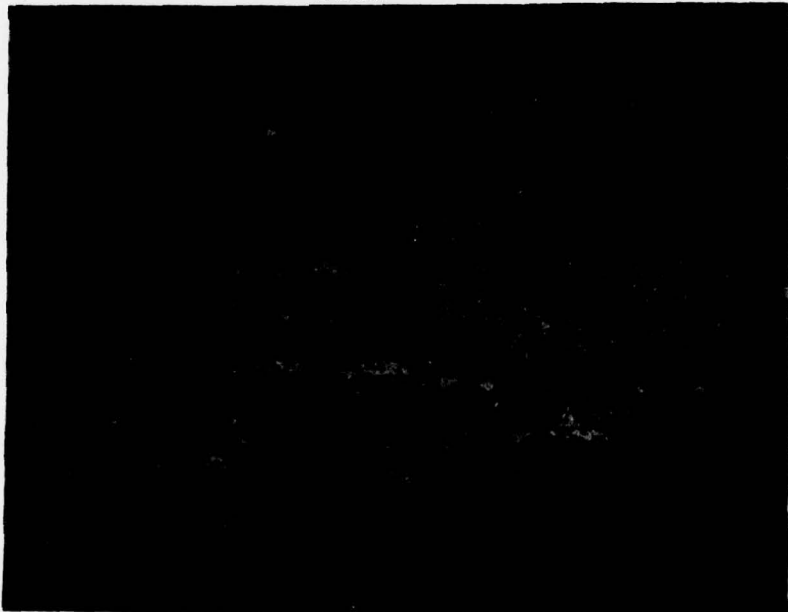
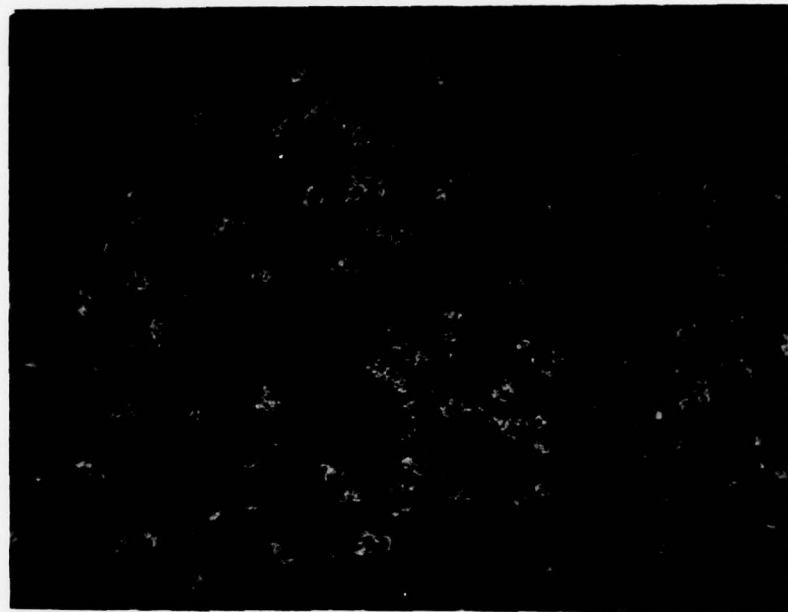


Figure 14d - Low Magnification (4.5x) Appearance of  
Test Panel After 35 Days Exposure at 9 m/s

Flow →



**Figure 14e - Low Magnification (4.5x) Appearance of Test Panel After 35 Days Exposure at 6 m/s**

Flow →

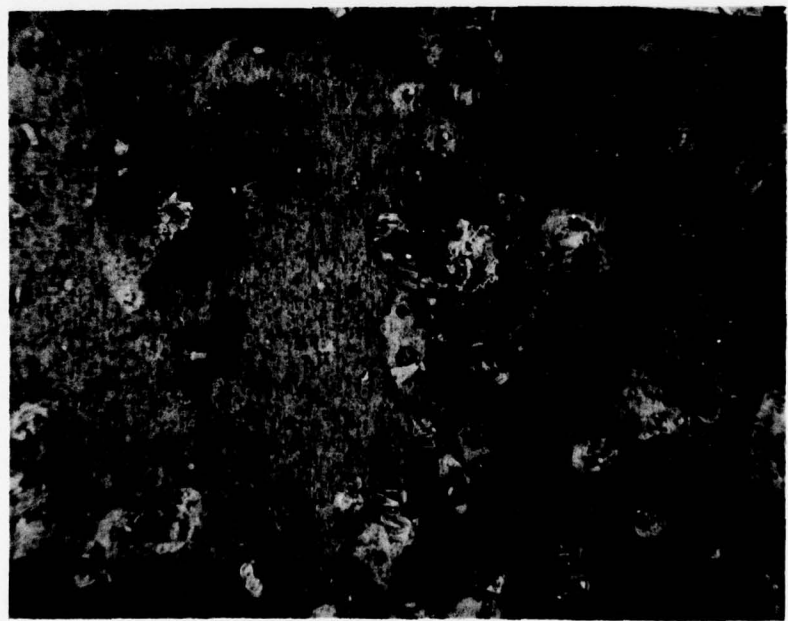


**Figure 14f - Low Magnification (4.5x) Appearance of Test Panel After 35 Days Exposure at 3 m/s**

Flow →

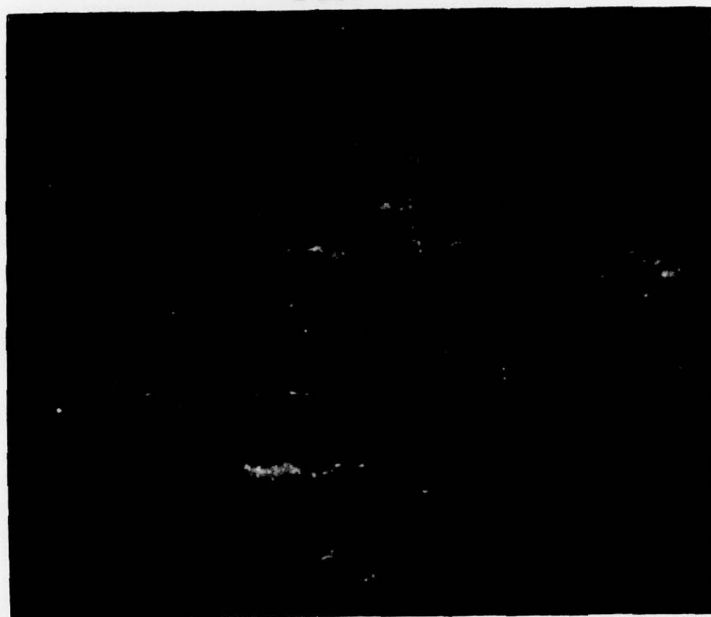


**Figure 15a - SEM Micrograph - 35 Days Exposure  
at 18 m/s (55x)**

Flow →

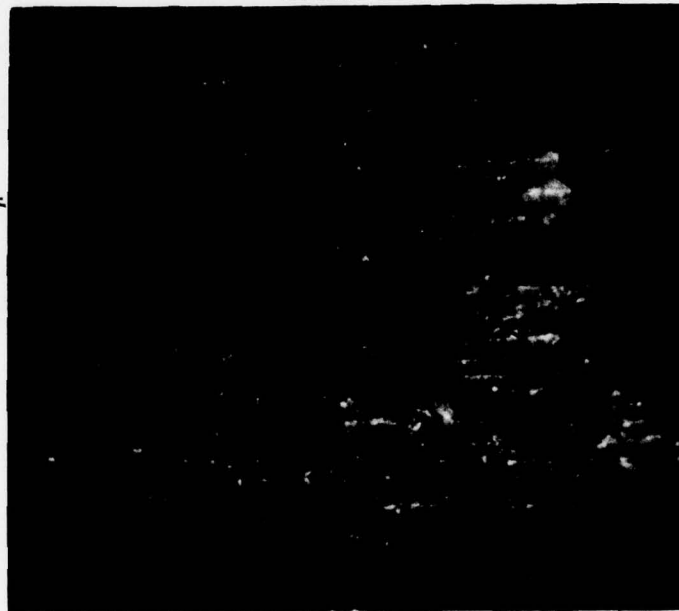


**Figure 15b - SEM Micrograph - 35 Days Exposure  
at 15 m/s (55x)**

Flow →



Figure 15c - SEM Micrograph - 35 Days Exposure  
at 12 m/s (55x)

Flow →



Figure 15d - SEM Micrograph - 35 Days Exposure  
at 9 m/s (55x)

Flow →

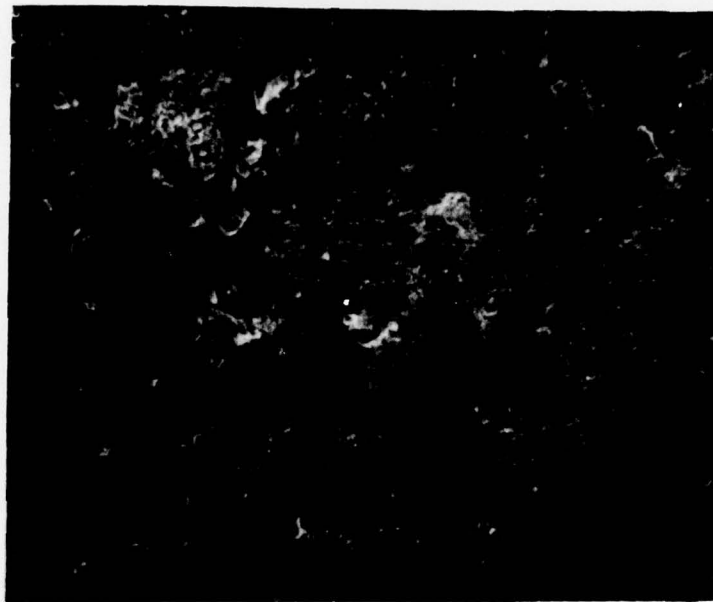


Figure 15e - SEM Micrograph - 35 Days Exposure  
at 6 m/s (55x)

Flow →



Figure 15f - SEM Micrograph - 35 Days Exposure  
at 3 m/s (55x)

Flow →

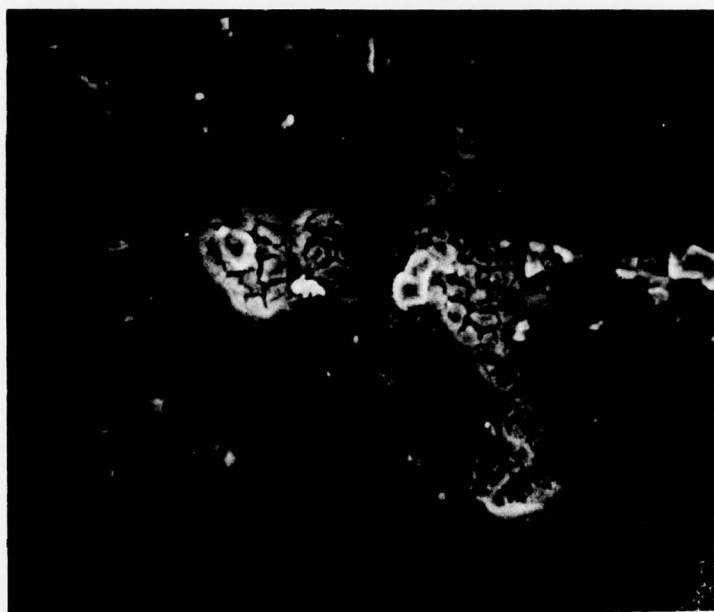


Figure 16 - SEM Micrograph - 35 Days  
Exposure at 18 m/s (1000x)

Flow →



Figure 17a - SEM Micrograph - 35 Days  
Exposure at 15 m/s (1000x)

Flow →

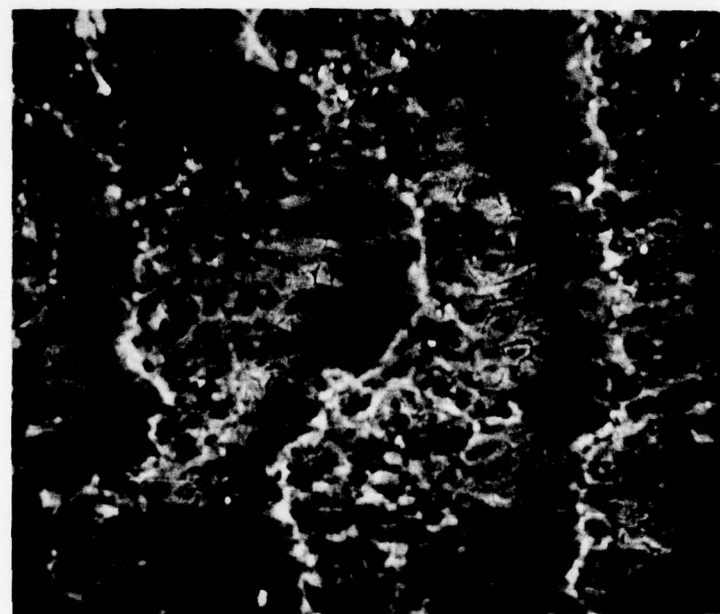


Figure 17b - SEM Micrograph - 35 Days  
Exposure at 15 m/s (1000x)

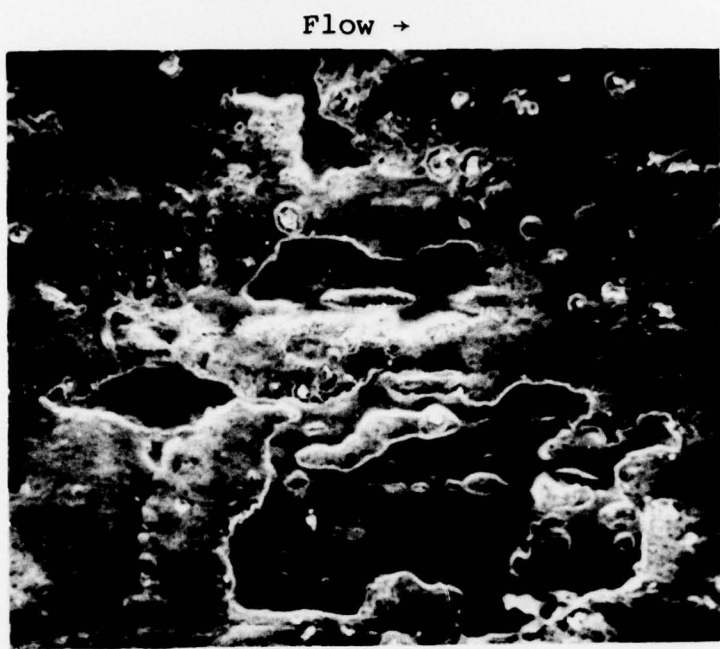


Figure 18a - SEM Micrograph - 35 Days  
Exposure at 12 m/s (300x)

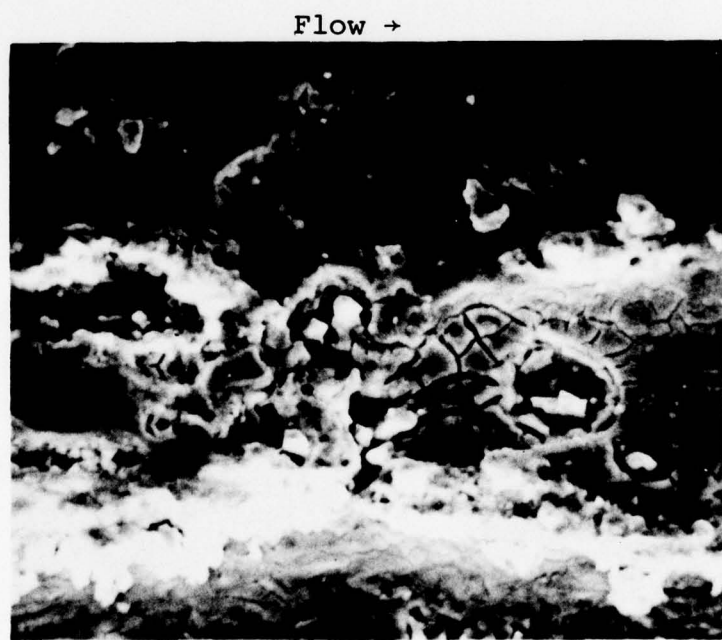


Figure 18b - SEM Micrograph - 35 Days  
Exposure at 12 m/s (1000x)

Flow →

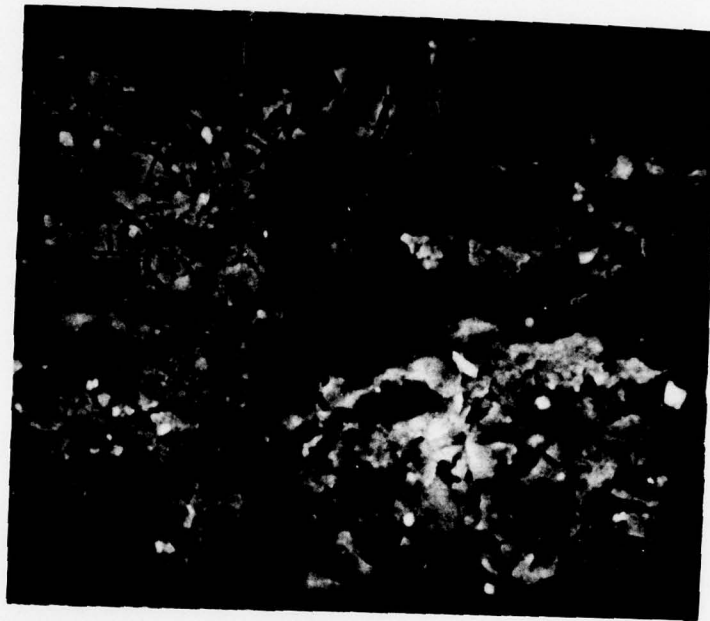


Figure 19 - SEM Micrograph - 35 Days  
Exposure at 6 m/s (1000x)

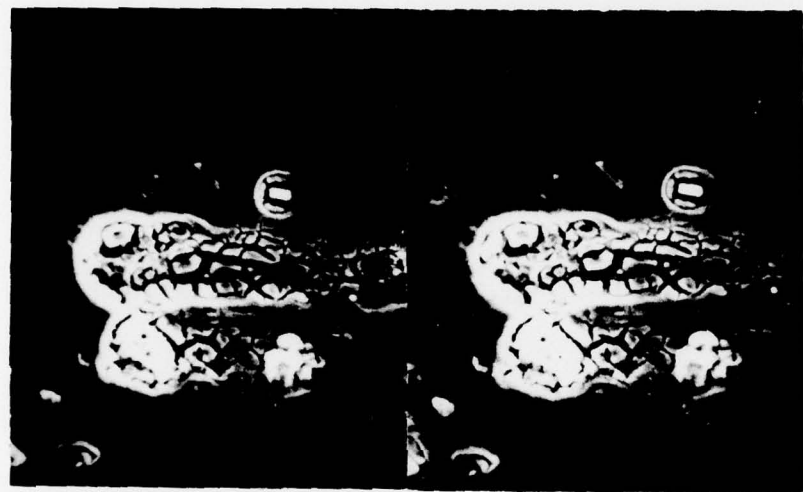


Figure 20 - SEM Stereo Micrograph Showing Preferential Pitting Downstream of Intermetallic Particles - 35 Days Exposure at 15 m/s (1000x)

Flow →

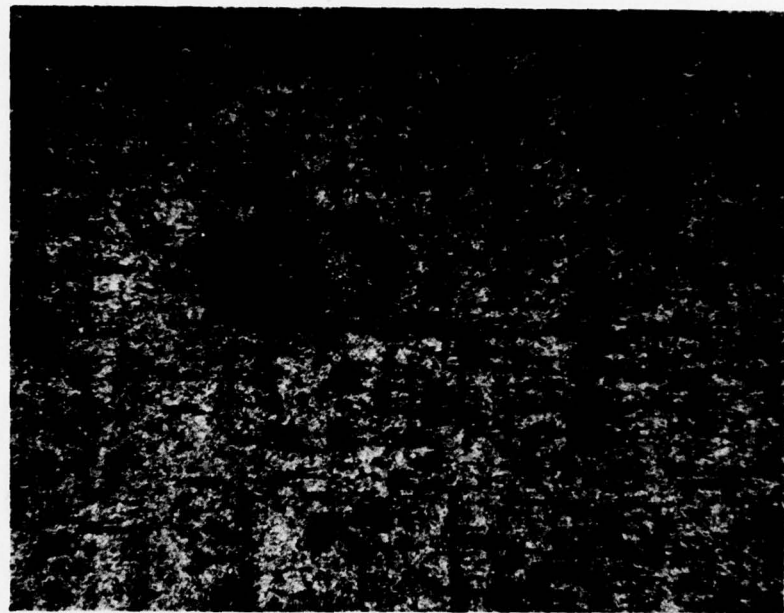


Figure 21 - Surface Appearance After  
22 Days Exposure at 30 m/s (125x)

Flow →

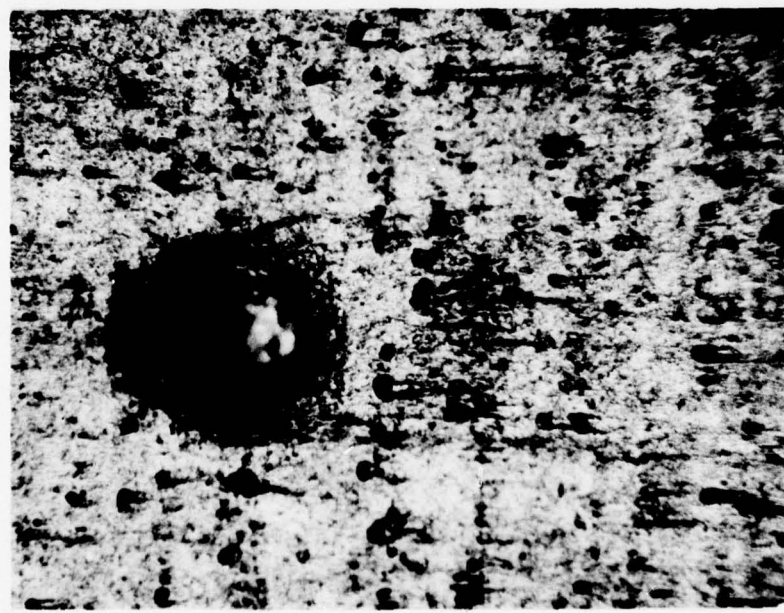


Figure 22 - Surface Appearance After  
22 Days Exposure at 30 m/s (250x)

Flow →

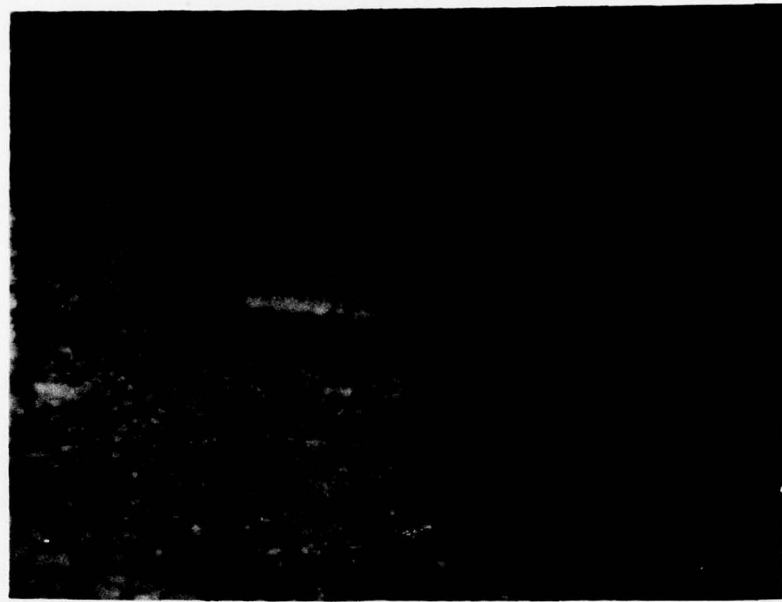


Figure 23 - Surface Appearance After  
22 Days Exposure at 30 m/s (1200x)

Flow →



Figure 24 - SEM Micrograph - 22 Days  
Exposure at 30 m/s (55x)

Flow →

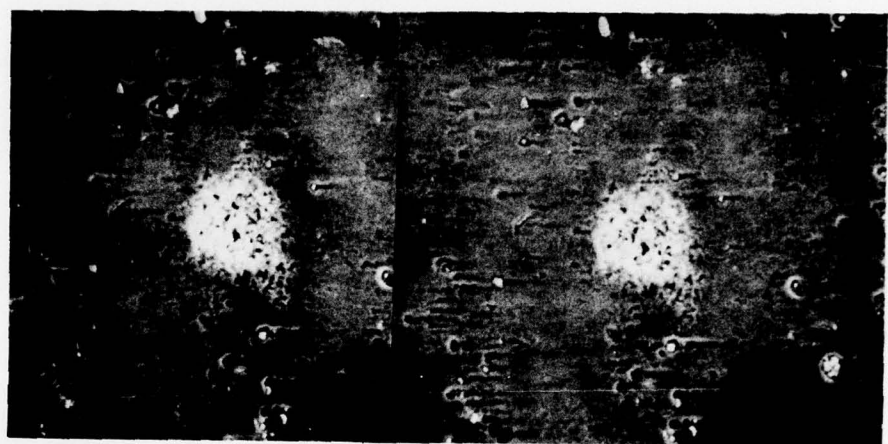


Figure 25 - SEM Stereo Micrograph Showing Random Macropit - 22 Days Exposure at 30 m/s (250x)

Flow →



Figure 26 - Higher Magnification (500x) SEM Stereo Micrograph of Figure 25

Flow →



Figure 27 - SEM Stereo Micrograph Showing Random Macropit - 22 Days Exposure at 30 m/s (250x)

Flow →

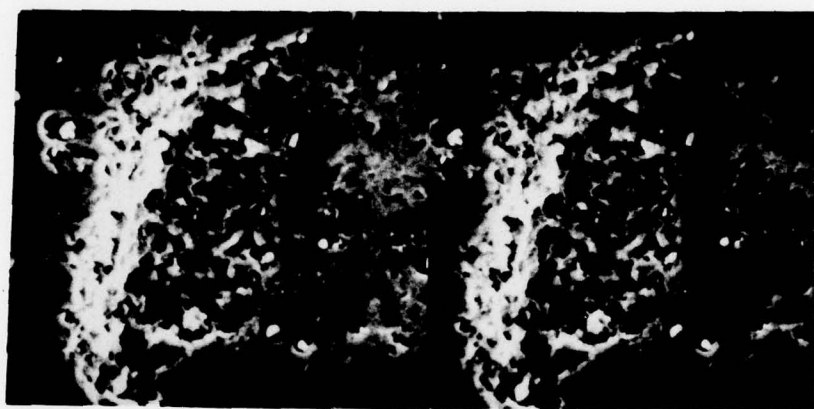


Figure 28 - Higher Magnification (500x) SEM  
Stereo Micrograph of Figure 27

Flow →

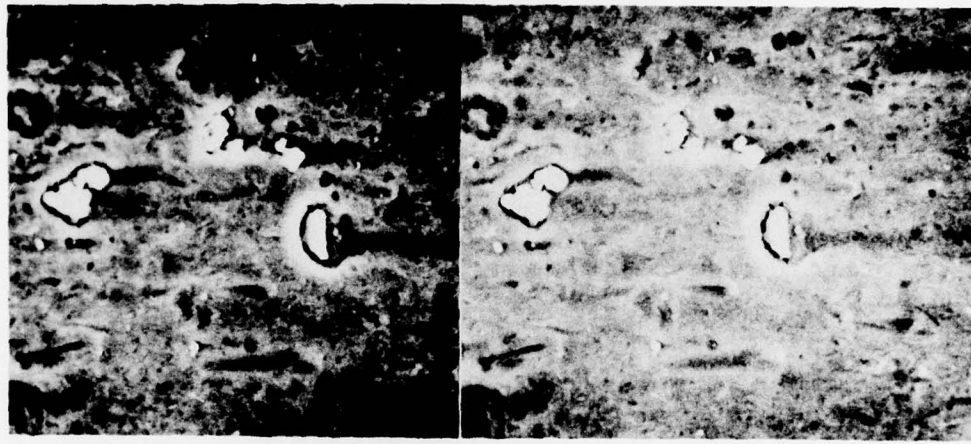


Figure 29 - SEM Stereo Micrograph Showing Micro-pitting and Preferential Attack Downstream of Intermetallic Particles - 22 Days Exposure at 30 m/s (1000x)

Flow →

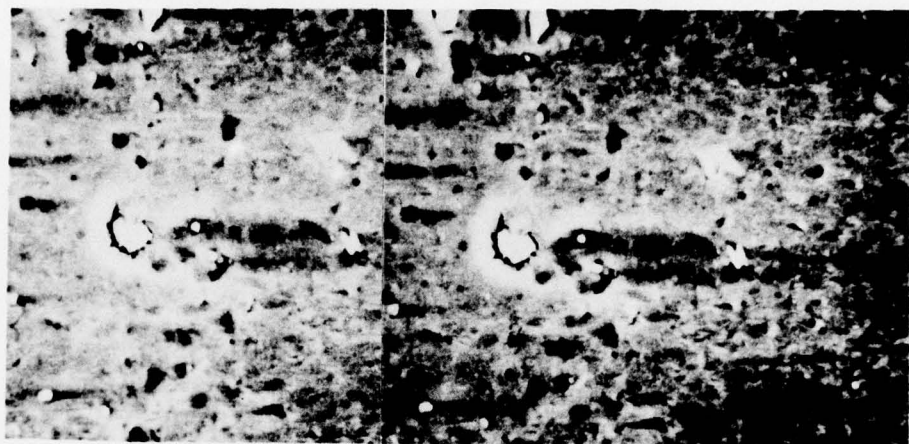
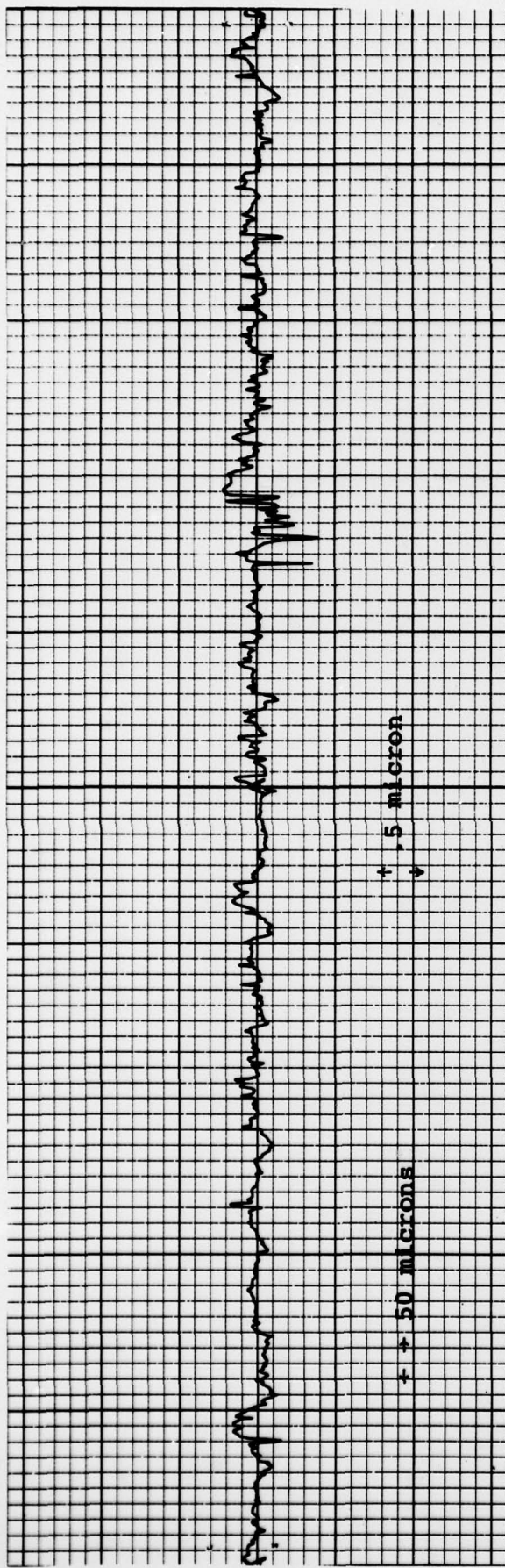


Figure 30 - SEM Stereo Micrograph Showing Micro-pitting and Preferential Attack Downstream of Intermetallic Particles - 22 Days Exposure at 30 m/s (1000x)

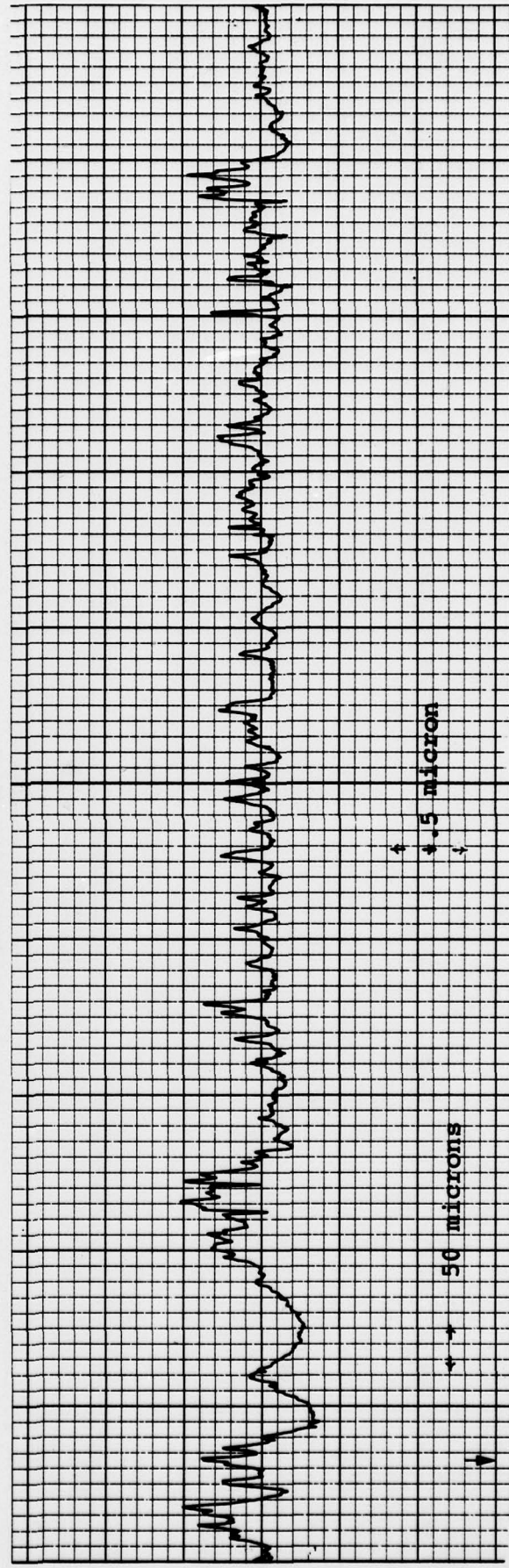
Flow →



Figure 31 - Higher Magnification (3000x) SEM  
Stereo Micrograph of Figure 30

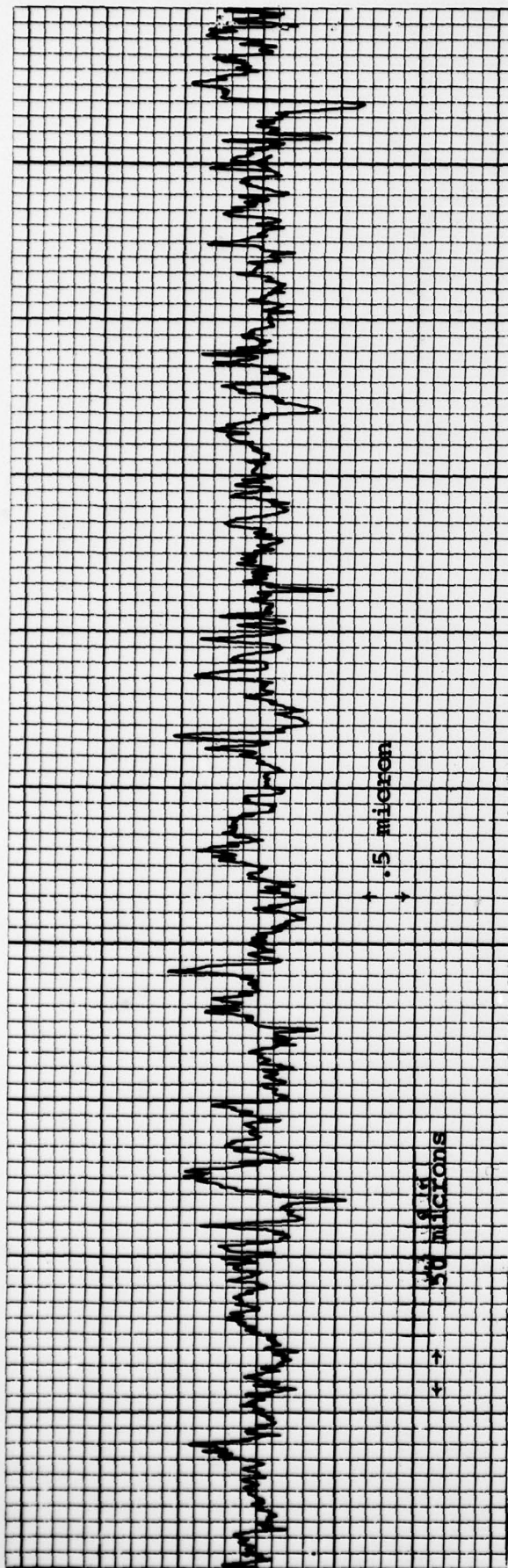


(a) Unexposed Control

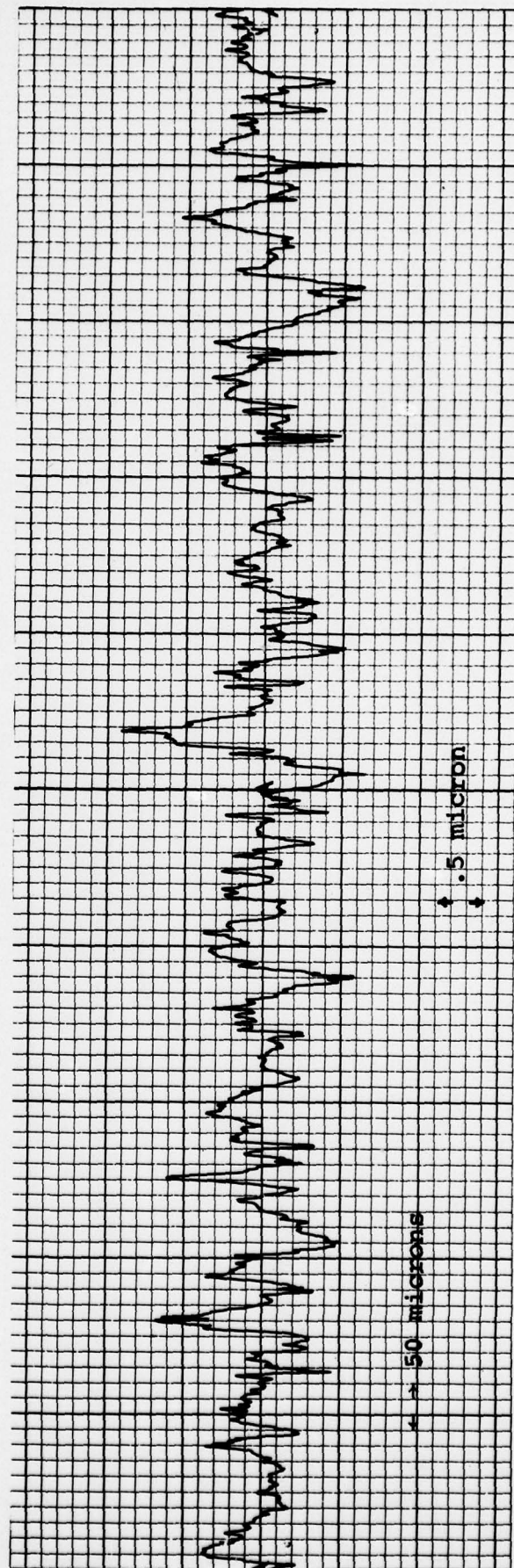


(b) Test Panel Exposed for 35 Days to  
Sea Water at 18 m/sec

Figure 32 - Surface Profile Trace with Stylus  
Traversing Parallel to Rolling Direction



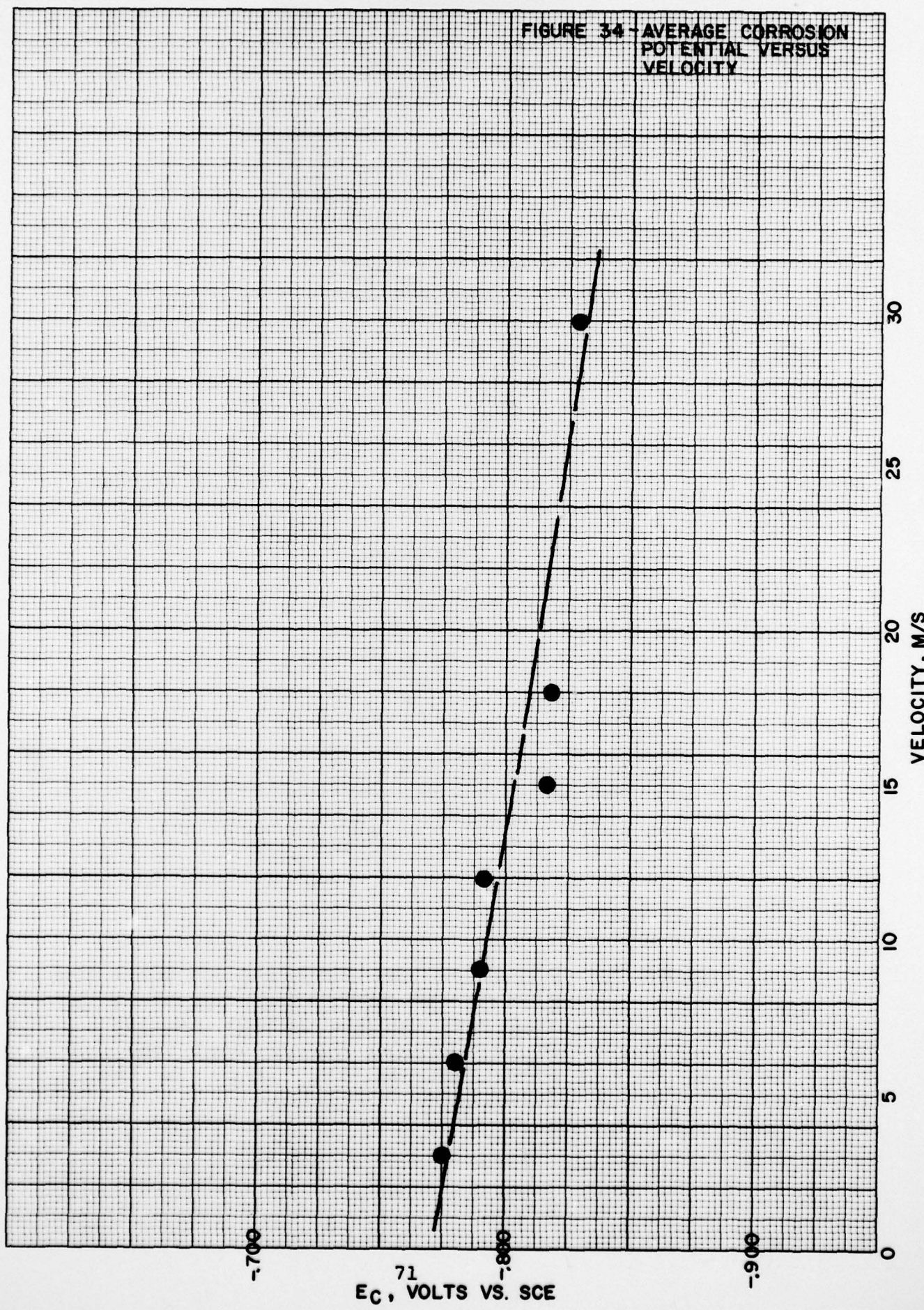
(a) Unexposed Control



(b) Test Panel Exposed for 35 Days to  
Sea Water at 18 m/sec

Figure 33 - Surface Profile Trace with Stylus  
Traversing Perpendicular to Rolling Direction

FIGURE 34 - AVERAGE CORROSION POTENTIAL VERSUS VELOCITY



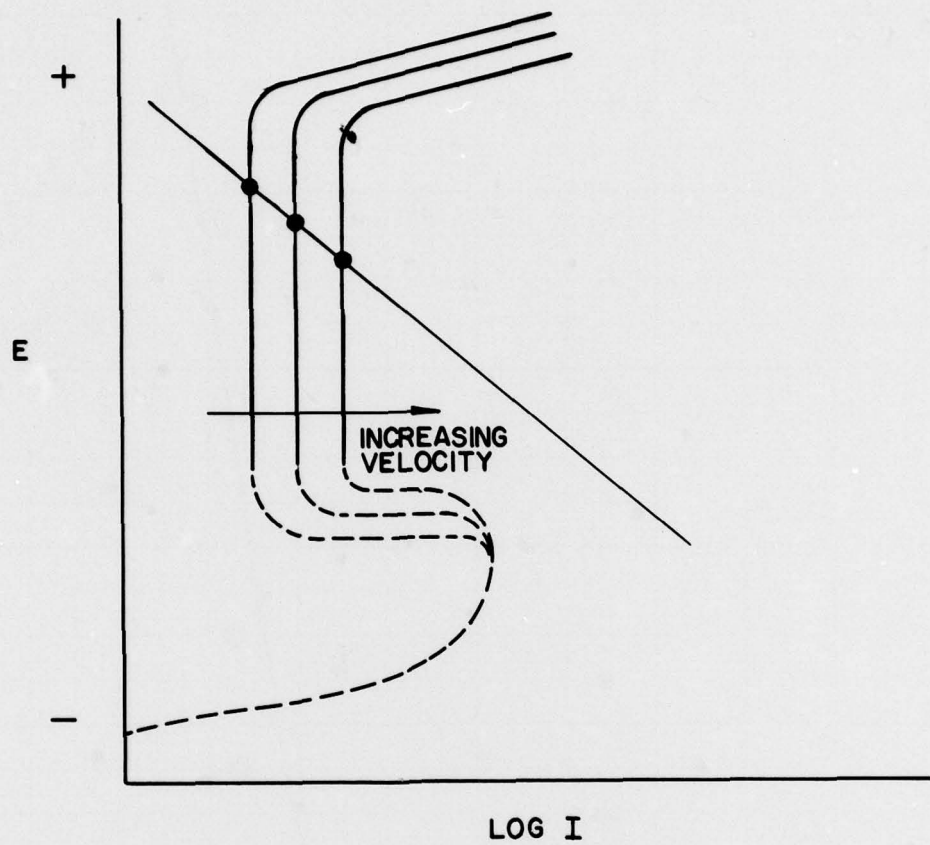


**FIGURE 35 - POLARIZATION DIAGRAM SHOWING THE EFFECT OF INCREASING VELOCITY ON THE DIFFUSION-LIMITED ANODIC POLARIZATION CURVE AND THE RESULTING ACTIVE SHIFT IN THE CORROSION POTENTIAL**

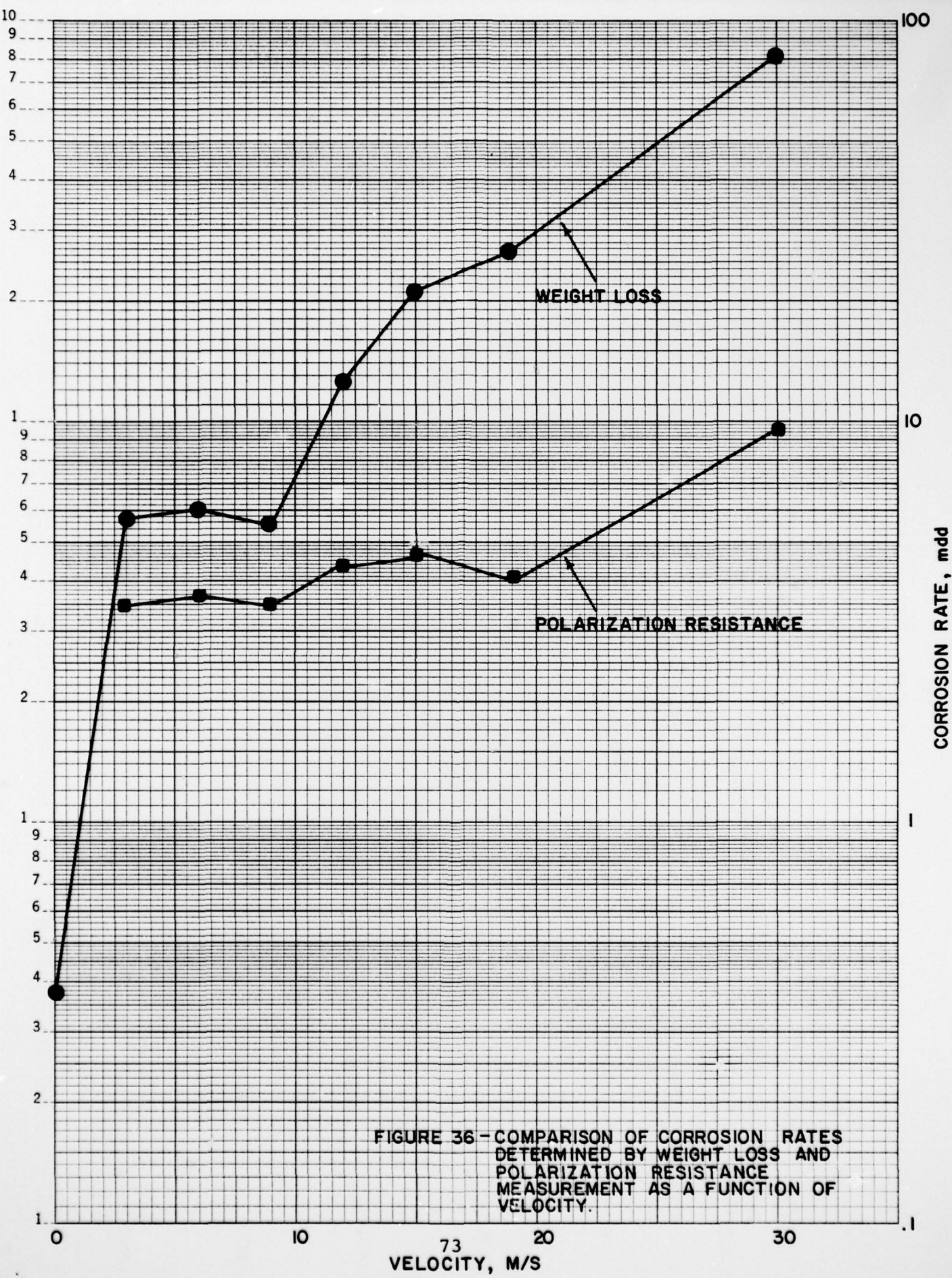


FIGURE 36 - COMPARISON OF CORROSION RATES DETERMINED BY WEIGHT LOSS AND POLARIZATION RESISTANCE MEASUREMENT AS A FUNCTION OF VELOCITY.

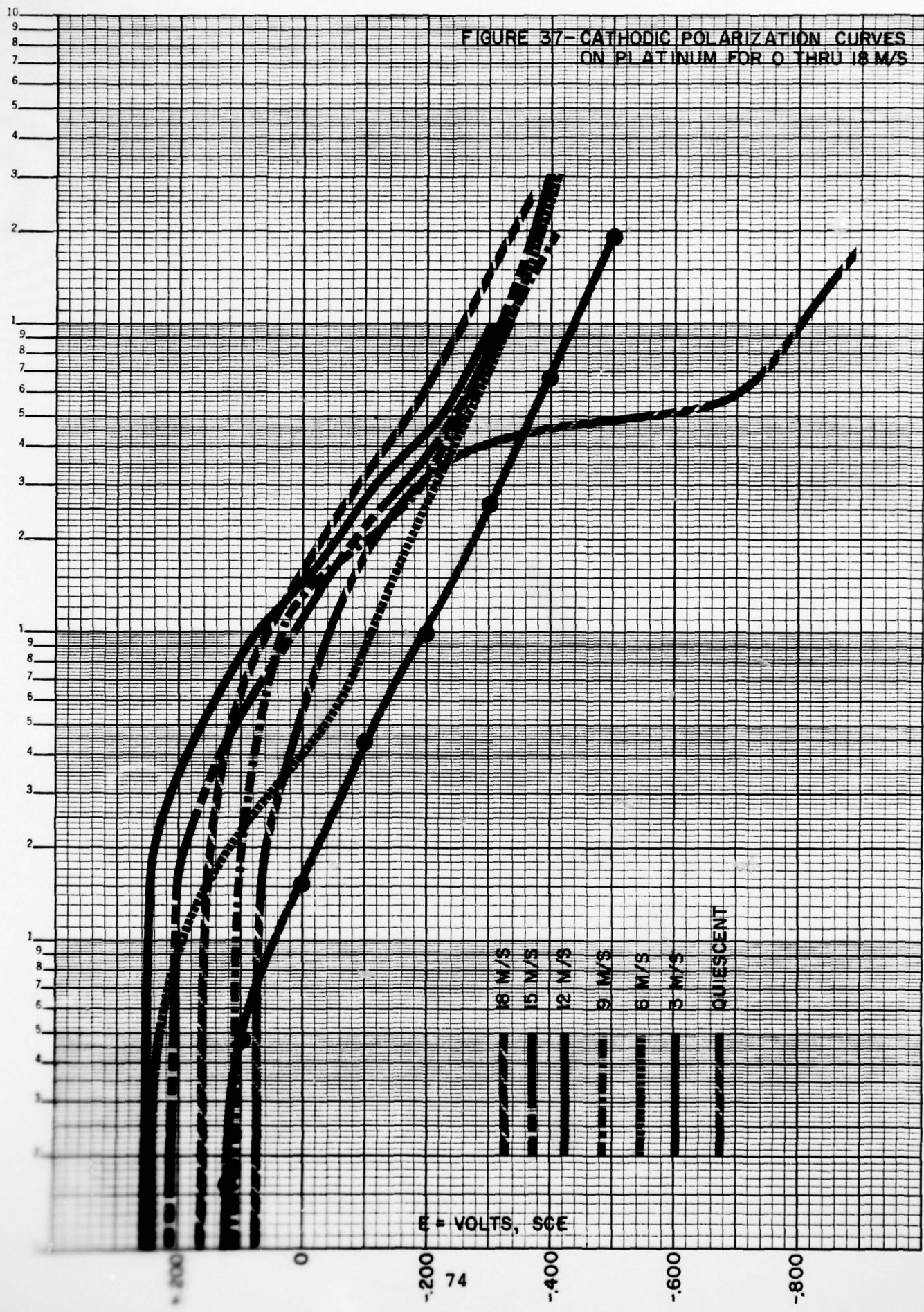


FIGURE 38 - COMPARISON OF CORROSION RATES DETERMINED IN FLOW CHANNEL VERSUS WATER WHEEL.

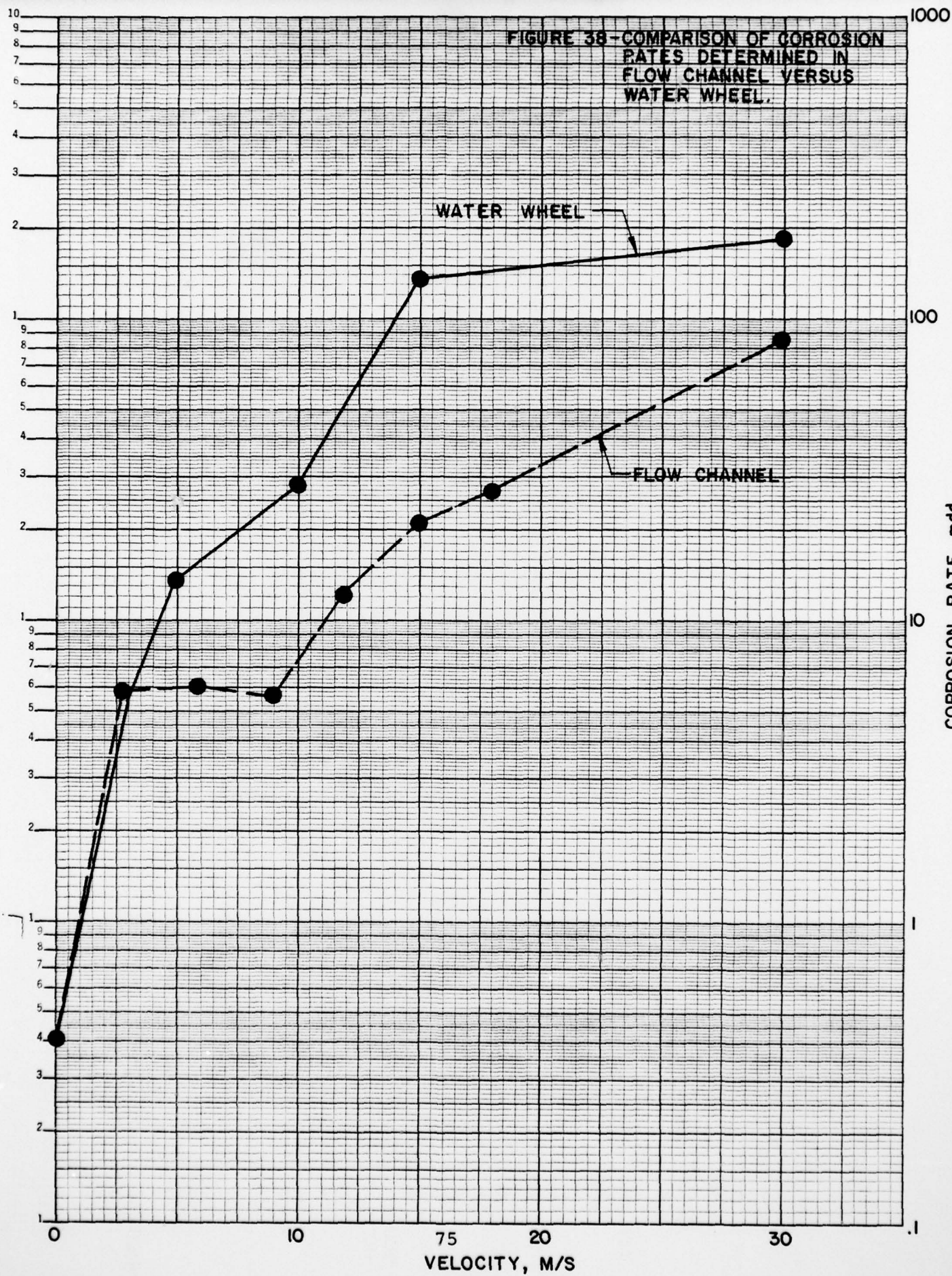
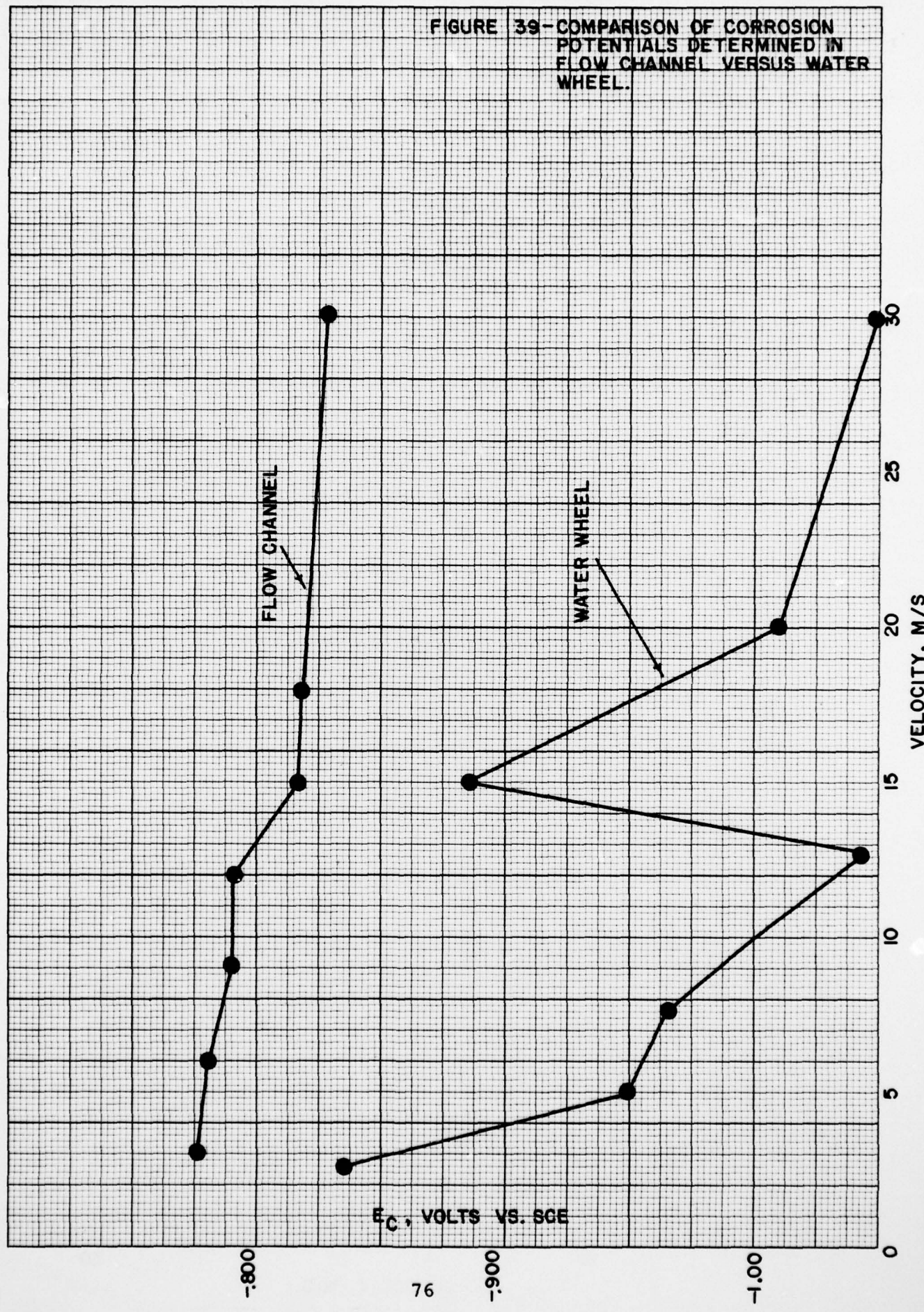


FIGURE 39 - COMPARISON OF CORROSION POTENTIALS DETERMINED IN FLOW CHANNEL VERSUS WATER WHEEL.

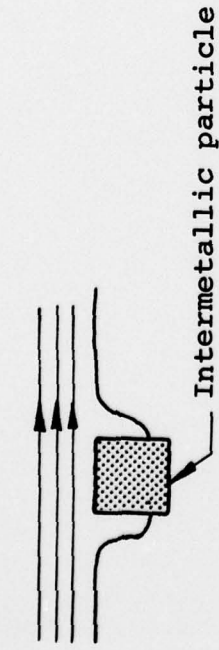


E<sub>c</sub>, VOLTS VS. SGE

Figure 40 - High Velocity Corrosion/Erosion of 5456-H117 Aluminum

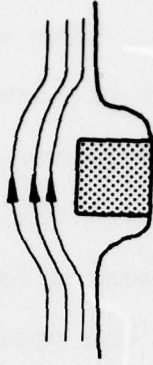
Step 1

Pitting initiates in a uniform mode about an intermetallic particle due to galvanic action.



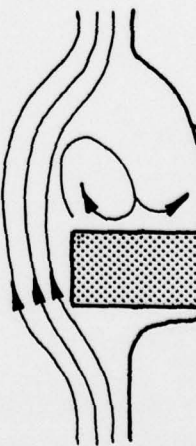
Step 2

As a result of localized pitting combined with general surface attack, the intermetallic particle begins to protrude into the flow stream.



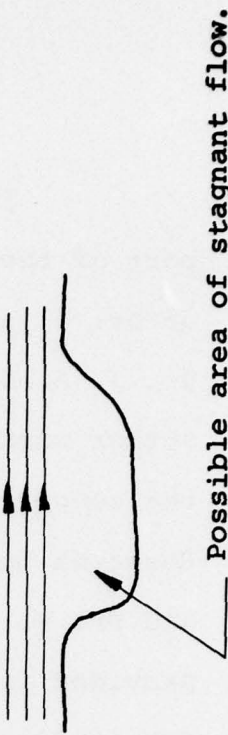
Step 3

This gives rise to greater turbulence immediately downstream of the particle and consequently, the pitting rate in this area accelerates.



Step 4

Eventually, the intermetallic particle is sufficiently undermined by corrosion that the hydrodynamic forces are sufficient to "pop" the particles from the matrix. Pitting corrosion in the remaining "hole" then slows down because of the loss of the particle and because of possible flow stagnation in the hole. Gradually, a uniform profile is reestablished. Macroscopically, this accounts for the very uniform loss of metal as corrosion/erosion proceeds.



#### ACKNOWLEDGEMENT

The author gratefully acknowledges the financial support of the Office Of Naval Research under the project supervision of Dr. P. A. Clarkin; the valued advice and consultation of Dr. J. A. Davis, Allegheny Ludlum Corporation, with whom the author worked for the past 5 years on much of the previous work; the cooperation and assistance of Mr. M. L. Peterson, Naval Research Laboratory, with whom much of this work was coordinated; and Dr. V. J. Damiano, Franklin Institute Research Labs, who provided invaluable assistance in conducting the profilometry and SEM studies.